ORIGINAL PAPER

CrossMark

Unravelling the antitumoral potential of novel bis(thiosemicarbazonato) Zn(II) complexes: structural and cellular studies

Elisa Palma[1,2] · Hugo M. Botelho[3] · Goreti Ribeiro Morais[1,4] · Inês Rodrigues[1] · Isabel Cordeiro Santos[1] · Maria Paula Cabral Campello[1] · Paula Raposinho[1] · Ana Belchior[1] · Susana Sousa Gomes[1] · Maria Fátima Araújo[1] · Isabel Correia[2] · Nadia Ribeiro[2] · Sofia Gama[1,5] · Filipa Mendes[1] · António Paulo[1]

Abstract

The development of pharmacologically active compounds based on bis(thiosemicarbazones) (BTSC) and on their coordination to metal centers constitutes a promising field of research. We have recently explored this class of ligands and their Cu(II) complexes for the design of cancer theranostics agents with enhanced uptake by tumoral cells. In the present work, we expand our focus to aliphatic and aromatic BTSC Zn(II) complexes bearing piperidine/morpholine pendant arms. The new complexes **ZnL^1–ZnL^4** were characterized by a variety of analytical techniques, which included single-crystal X-ray crystallography for **ZnL^2** and **ZnL^3**. Taking advantage of the fluorescent properties of the aromatic complexes, we investigated their cellular uptake kinetics and subcellular localization. Furthermore, we tried to elucidate the mechanism of action of the cytotoxic effect observed in human cancer cell line models. The results show that the aliphatic complexes (**ZnL^1** and **ZnL^2**) have a symmetrical structure, while the aromatic counterparts (**ZnL^3** and **ZnL^4**) have an asymmetrical nature. The cytotoxic activity was higher for the aromatic BTSC complexes, as well as the cellular uptake, evaluated by measurement of intracellular Zn accumulation. Among the most active complexes, **ZnL^3** presented the fastest uptake kinetics and lysosomal localization assessed by live-cell microscopy. Detailed studies of its impact on cellular production of reactive oxygen species and impairment of lysosomal membrane integrity reinforced the influence of the pendant piperidine in the biological performance of aromatic BTSC Zn(II) complexes.

Keywords Zinc · Bis(thiosemicarbazones) · X-ray diffraction · Fluorescence imaging · Cellular studies

Introduction

Thiosemicarbazones (TSC) and bis(thiosemicarbazones) (BTSC), as well as their metal complexes, have received considerable attention in the design of new drugs against a range of diseases due to their broad pharmacological activity

✉ Filipa Mendes
  fmendes@ctn.tecnico.ulisboa.pt

✉ António Paulo
  apaulo@ctn.tecnico.ulisboa.pt

1   Centro de Ciências e Tecnologias Nucleares, Instituto Superior Técnico, Universidade de Lisboa, Estrada Nacional 10 (km 139,7), 2695-066 Bobadela LRS, Portugal

2   Centro Química Estrutural, Instituto Superior Técnico, Universidade de Lisboa, Av. Rovisco Pais, 1049-001 Lisbon, Portugal

3   BioISI—Biosystems and Integrative Sciences Institute, University of Lisboa, Faculty of Sciences, Campo Grande, C8, 1749-016 Lisbon, Portugal

4   Present Address: Institute of Cancer Therapeutics, Faculty of Life Sciences, University of Bradford, Bradford BD7 1DP, UK

5   Present Address: Institut für Anorganische und Analytische Chemie, Friedrich-Schiller-Universität Jena, Humboldtstr. 8, 07743 Jena, Germany

Springer

that includes antibacterial, antimalarial, antiviral, and antitumoral properties [1–4]. In addition, bis(thiosemicarbazones) also present a strong potential for cancer theranostics, since they can form complexes with different di- or trivalent metals relevant in the biomedical imaging field. This comprises complexes with radiometals suitable for in vivo clinical imaging by PET (positron emission tomography) (e.g., ^{64}Cu or ^{68}Ga) or SPECT (single-photon emission computed tomography) (e.g., ^{111}In), as well as fluorescent Zn(II) complexes for preclinical studies using optical imaging modalities (e.g., fluorescence microscopy) [5].

The intense research efforts on the chemistry of TSC and BTSC derivatives and their metal complexes have already led to achievements with clinical translational potential. The most prominent example is the Cu(II) complex CuATSM (ATSM = diacetyl-bis(N^4-methylthiosemicarbazonate)) that, when prepared with the positron-emitting ^{64}Cu, has been thoroughly investigated as a PET tracer to image hypoxia in tumors and cardiac ischemia. After initial clinical trials, ^{64}CuATSM was successfully evaluated in patients with different tumors (e.g., lung, cervical, and rectal cancers) providing useful clinical data [6–8]. More recently, DpC (di-2-pyridylketone 4-cyclohexyl-4-methyl-3-thiosemicarbazone), which belongs to the di-2-pyridylketone thiosemicarbazone class of compounds, has also entered Phase 1 multicenter clinical trials as an anticancer agent to treat advanced and resistant tumors [3]. Like other TSC derivatives, DpC has a polypharmacological profile, which comprises the ability to bind iron and copper ions with consequent generation of intracellular reactive oxygen species (ROS) that ultimately lead to lysosomal membrane permeabilization (LMP) and cell death [3, 9–13].

Inspired by these encouraging progresses, we have recently reported the synthesis and biological evaluation of a new family of BTSC copper(II) complexes [14]. These new compounds were designed based on the functionalization of the CuATSM scaffold with pendant cyclic amines (piperidine and morpholine) introduced at the exocyclic nitrogen atoms, using appropriate methylenic linkers. We envisaged that the presence of the cyclic amine side chains could have a positive effect on the water solubility of the complexes, a crucial issue in the design of metal-based anticancer drugs, without compromising their ability to accumulate in tumoral cells and induce cytotoxic effects. Moreover, the presence of the piperidine and morpholine rings could also influence the intracellular distribution of the complexes, namely, by promoting its lysosomal entrapping [15, 16].

Our previous work proved that piperidinyl/morpholinyl derivatives of CuATSM present a significant cytotoxic activity against a panel of human tumoral cell lines, showing a remarkably higher uptake than CuATSM in most tumoral cells studied [14]. To further evaluate how the presence of the pendant cyclic amines influences the cellular uptake, subcellular localization, and the possible mechanism of action for this class of BTSC M(II) complexes, we have extended the studies to Zn(II) congeners. BSTC Cu(II) complexes typically show poor fluorescence properties, since Cu(II) is a d^9 paramagnetic metal center that tends to quench the emission of fluorescence [17]. In opposition, BTSC Zn(II) complexes usually present fluorescence properties suitable for the follow-up of their cell uptake kinetics and subcellular localization by fluorescence microscopy [17, 18].

For the studies with the BTSC Zn(II) complexes bearing piperidine/morpholine pendant arms, we have focused on derivatives of ZnATSM and ZnNqTSM (NqTSM = bis[4-N-methyl-3-thiosemicarbazone] acenaphthenequinone), as shown in Fig. 1. By studying ZnNqTSM derivatives containing a naphthalene-based aromatic backbone, we expected

Fig. 1 General structures of the **Zn^{II}ATSM** and **Zn^{II}NqTSM^{asym}** derivatives
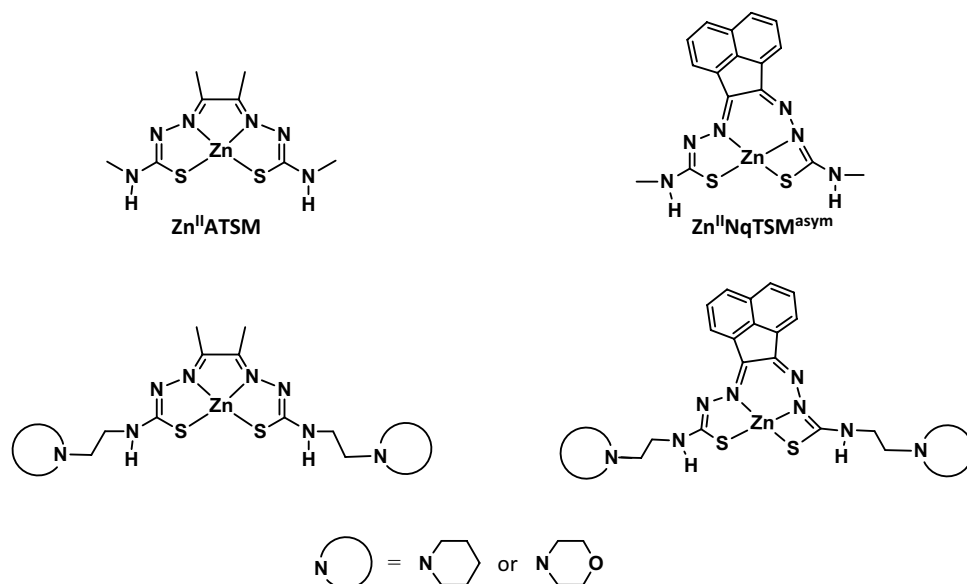
compounds with enhanced fluorescence properties and, therefore, more suited for live-cell imaging studies than the aliphatic counterparts. Pascu et al. showed previously that **ZnNqTSM** and its congener containing allyl groups at the exocyclic nitrogen atoms have more favorable fluorescence properties than **ZnATSM** due to the presence of the flat and aromatic naphthalene backbone. This feature allowed an easier monitoring of the cellular uptake and subcellular localization of the compounds [17].

In this contribution, we describe the synthesis, characterization, and in vitro biological evaluation of this new family of BTSC Zn(II) complexes. The in vitro biological evaluation included a variety of studies on a panel of human tumoral cell line models, namely, the assessment of their cytotoxic properties and the quantification of their cellular uptake by ICP-MS measurement of intracellular Zn. For the aromatic complexes, i.e., those derived from **Zn^{II}NqTSM^{asym}**, their biological evaluation was also performed with live-cell imaging assays to study their cellular uptake kinetics and for subcellular localization. The ability of selected aromatic compounds to induce lysosomal membrane permeabilization (LMP) and generate intracellular ROS was also evaluated, to gain some insight on their mechanism of action. As a comparison, some of these studies were also conducted for the parental compounds, **ZnATSM** and **ZnNqTSM^{asym}**, searching for a better understanding of the influence of different structural features (presence and type of cyclic amine pendant arms or aliphatic vs aromatic ligand backbone) on the biological performance of the compounds.

Results and discussion

Synthesis

The synthesis of Zn(II) complexes with aliphatic bis(thiosemicarbazone) ligands, namely, **ATSM** derivatives, is commonly described in the literature by reacting the appropriate ligands with Zn(II) salts.[5] By contrast, the reported aromatic congeners of the **Zn^{II}NqTSM** type have been obtained by template reactions between acenaphthenequinone with the desired thiosemicarbazide in the presence of a zinc salt [17, 18]. In our case, the first approach was used to obtain both the aliphatic or aromatic Zn(II) complexes; therefore, the work was initiated with the synthesis of the different chelators, i.e., **ATSM**, **NqTSM**, and the corresponding derivatives (**H$_2$L^1**–**H$_2$L^4**) carrying piperidine and morpholine pendant arms (Scheme 1).

The previously reported aliphatic chelators **H$_2$ATSM**, **H$_2$L^1**, and **H$_2$L^2** were obtained by an acetic acid-catalyzed condensation reaction between 2,3-butanedione and the respective 4-substituted thiosemicarbazides (**1-3**), as described elsewhere [14]. As shown in Scheme 1, the aromatic counterparts **H$_2$L^3** and **H$_2$L^4** were synthesized using a similar methodology by refluxing acenaphthenequinone with the corresponding thiosemicarbazide but in the presence of hydrochloric acid. **H$_2$L^3** and **H$_2$L^4** are new compounds that were obtained with moderate yields
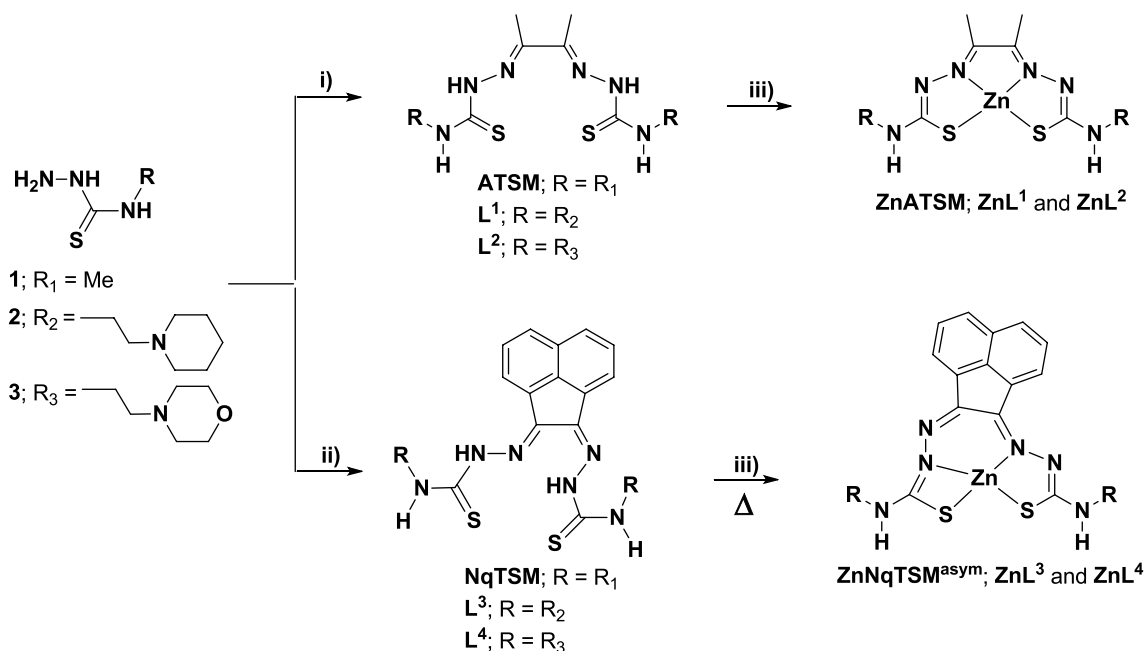
Scheme 1 Synthesis of the BTSC chelators and respective Zn(II) complexes. (i) 2,3-butanedione, 5% acetic acid, 60 °C; (ii) acenaphthenequinone, HCl 2 N, ethanol, reflux; and (iii) Zn(OAc)$_2$.2H$_2$O, MeOH

of 53 and 65%, respectively. Recently, Pascu et al. have used a microwave-assisted reaction to prepare aromatic bis(thiosemicarbazones), including the **H₂NqTSM** chelator that was obtained in a very high yield (95%) [19]. According to the authors, this microwave-assisted procedure presents the advantage of requiring very short reaction times to produce almost quantitative amounts of the aromatic BTSCs. The shorter reaction time minimizes the occurrence of side reactions, namely, the cyclization of the starting thiosemicarbazides that result in the formation of impurities and render the purification of the final chelators more demanding. Although being synthesized by a conventional acid-catalyzed reaction, **H₂L³** and **H₂L⁴** could be purified in a straightforward way by column chromatography and were obtained with reasonable yields. For this reason, we did not proceed with the optimization of their synthesis using microwave-assisted reactions.

The new Zn^{II}BTSC complexes (**ZnL¹** to **ZnL⁴**) were obtained in moderately high yields (70–76%) by reacting hydrated zinc acetate with one equivalent of the corresponding ligand in methanol, as depicted in Scheme 1. The same methodology was used to synthesize the Zn(II) complex of **NqTSM** containing an asymmetrically coordinated ligand (see discussion below). This complex is herein designated as **ZnNqTSM^{asym}** to distinguish from the previously reported **ZnNqTSM** complex obtained based on the template method, which contains a symmetrically coordinated BTSC.[18] All these Zn(II) complexes, except **ZnL³**, precipitate from the respective reaction mixtures as yellow–orange microcrystalline powders. For **ZnL³**, the solvent of the reaction mixture was evaporated in vacuum and the yellow–orange complex was obtained in a pure form after recrystallization in a mixture of dichloromethane and diethyl ether.

The characterization of the BTSC chelators and their zinc complexes was done by ESI–MS, elemental analysis (CHN), ^{1}H, and ^{13}C NMR and IR spectroscopy (see the experimental part). Single crystals were obtained for **ZnL²** and **ZnL³**, which allowed the determination of their solid-state structures by X-ray crystallography analysis.

NMR spectroscopy

For the aliphatic BTSC Zn(II) complexes, **ZnL¹** and **ZnL²**, the splitting pattern and relative areas of the peaks present in their ^{1}H NMR spectra show that the BTSC chelators are coordinated in a symmetric way, by the two inner imine nitrogen atoms and the two thiolate sulfur atoms. This mode of coordination was confirmed in the X-ray structure of **ZnL²**, as described below. The symmetric coordination of the aliphatic chelators in **ZnL¹** and **ZnL²** was evident by the presence of a singlet at 2.18 ppm, integrating for six protons (CH₃ groups in the ethylenic bridge), and a broad singlet at 6.98–7.35 ppm, integrating for two protons (N–H groups).

Each type of CH₂ and CH₃ groups from the two alkyl linkers and two amine rings is also chemically equivalent and gives raise to resonances integrating to four or six protons, respectively, being observed a few occasional overlaps. Consistently, the ^{13}C NMR spectra of **ZnL¹** and **ZnL²** exhibit a single resonance for each set of equivalent of carbon atoms of the two thiosemicarbazone units and ethylenic bridge. The coordination of **H₂L¹** and **H₂L²** as dianionic and tetradentate N₂S₂ chelators was further corroborated by the absence of the resonance due to the acidic NH protons that appear in the spectra of the free ligands at ca. 10.4 ppm.

Contrarily to the aliphatic compounds, **ZnNqTSM^{asym}**, **ZnL³** and **ZnL⁴**, and the corresponding free ligands (**H₂NqTSM**, **H₂L³**, and **H₂L⁴**) present ^{1}H and ^{13}C NMR spectra with splitting patterns compatible with an asymmetric structure for the aromatic BTSCs. This is clearly seen by the presence of two resonances for the NH hydrazone protons in the ^{1}H NMR spectra of the free ligands **H₂L³** and **H₂L⁴**, spanning between 11.30 and 12.86 ppm, and the presence of two resonances in the range 8.55–9.06 ppm due to the exocyclic NH protons (Figures S1 and S3). These results can be explained by the presence of *E* and *Z* pairs for each type of NH protons, as previously described for the **H₂NqTSM** chelator [19]. Moreover, **H₂L³** and **H₂L⁴** were obtained exclusively as (*E*,*Z*) isomers. The preference for the (*E*,*Z*) geometry might eventually reflect the minimization of the repulsion between the lone pairs from the imino-nitrogen atoms. The assignment of the different NH protons was performed by comparison with the chemical shifts exhibited by the same protons in **H₂NqTSM**. For each type of NH group, the *E* protons are upfield shifted when compared with their *Z* counterparts (see SI, Figures S1 and S3), as proposed for **H₂NqTSM** [19].

For the aromatic BTSC Zn(II) complexes (**ZnNqTSM^{asym}**, **ZnL³**, and **ZnL⁴**), each pair of H1/1', H2/2', and H3/3′ protons and corresponding carbon atoms gives rise to two independent resonances, except in a few occasional overlaps, as shown in Fig. 2, for **ZnL⁴**. This splitting pattern is less evident for the proton and carbon atoms from the cyclic amine pendant arms which, being farther away from the metal center, are less affected by the asymmetric coordination environment around Zn(II). The asymmetric tetradentate coordination of the aromatic BTSC chelator through the two sulfur atoms, one inner and one outer imine nitrogen atoms was confirmed by X-ray structural analysis in the case of **ZnL³**, as discussed below. The ^{1}H and ^{13}C NMR data collected for the aromatic Zn(II) complexes indicate that this asymmetric coordination mode is retained in solution for all the compounds.

The ^{1}H NMR spectra of **ZnL³**, **ZnL⁴**, and **ZnNqTSM^{asym}** showed well-defined and rather narrow resonances, whose profile did not change with time, indicating that the asymmetric Zn(II) complexes do not undergo dynamic

Fig. 2 ^{1}H and ^{13}C NMR spectra of **ZnL$_4$** in DMSO-d_6 in the N–$\underline{\text{H}}$ and aromatic regions
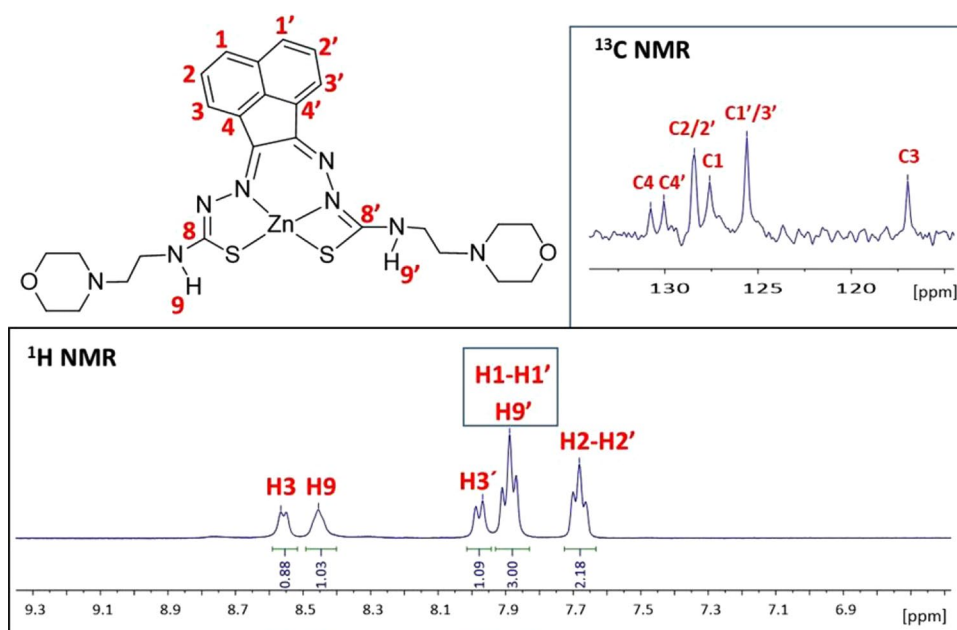
processes in solution, contrarily to the symmetric counterparts reported earlier by Pascu et al. [17]. Altogether, these results strongly suggest that the ligands **H$_2$L^3**, **H$_2$L^4**, and **H$_2$NqTSM**, in the (*E,Z*) conformation are pre-organized to coordinate the metal center through one inner and one outer imine nitrogen atoms, and consequently, the formation of asymmetric Zn(II) complexes is kinetically favored.

X-ray crystallography and mass spectrometry

Crystals of **ZnL^2** and **ZnL^3** were obtained by slow diffusion of diethyl ether into concentrated methanolic and dichloromethane solutions of the complexes, respectively. A summary of the crystallographic data is presented in Table S1 and the most relevant bond distances and angles are listed in Table S2 (SI). Single-crystal X-ray diffraction analysis

revealed that the complexes exist in the solid state as discrete monomeric or dimeric neutral molecules (Figs. 3 and 4).

In both compounds, the Zn(II) ion is pentacoordinated with a slightly distorted square-pyramidal geometry ($\tau = 0.103$ and $\tau = 0.100$ for **ZnL^2** and **ZnL^3**, respectively) [20]. In monomeric **ZnL^2**, the square-pyramidal coordination around the Zn^{2+} ion is ensured by the N1, N4, S1, and S2 atoms occupying the basal plane, and by the oxygen atom O3 from the water molecule at the axial position (Fig. 3). The Zn atom lies 0.549(1) Å above the basal plan towards the coordinated oxygen atom. The coordination of the aliphatic bis(thiosemicarbazone) ligand affords the formation of three fused five-membered chelate rings. The dihedral angle between the least-square (l.s.) plane of the ethylenic bridge C3–C2–C5–C6 and the l.s. plane of the central chelate ring C2–N1–Zn1–N4–C3 is 5.71(14)º, whereas the dihedral angles with the l.s. planes
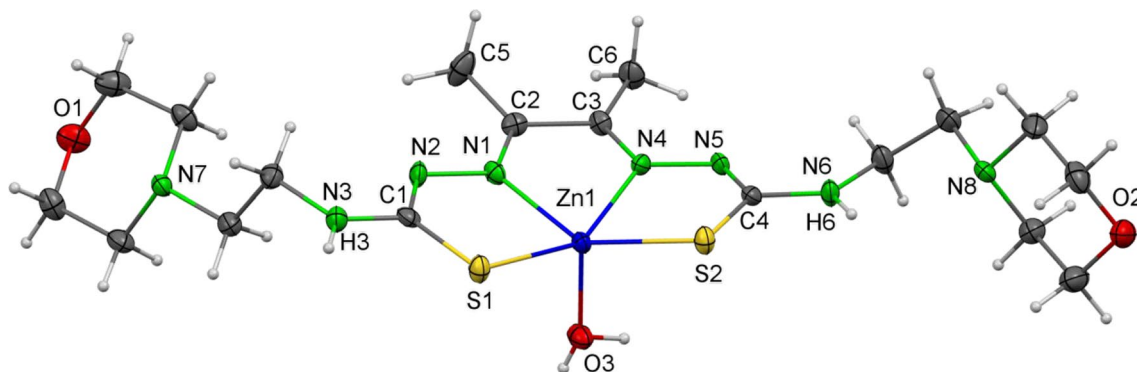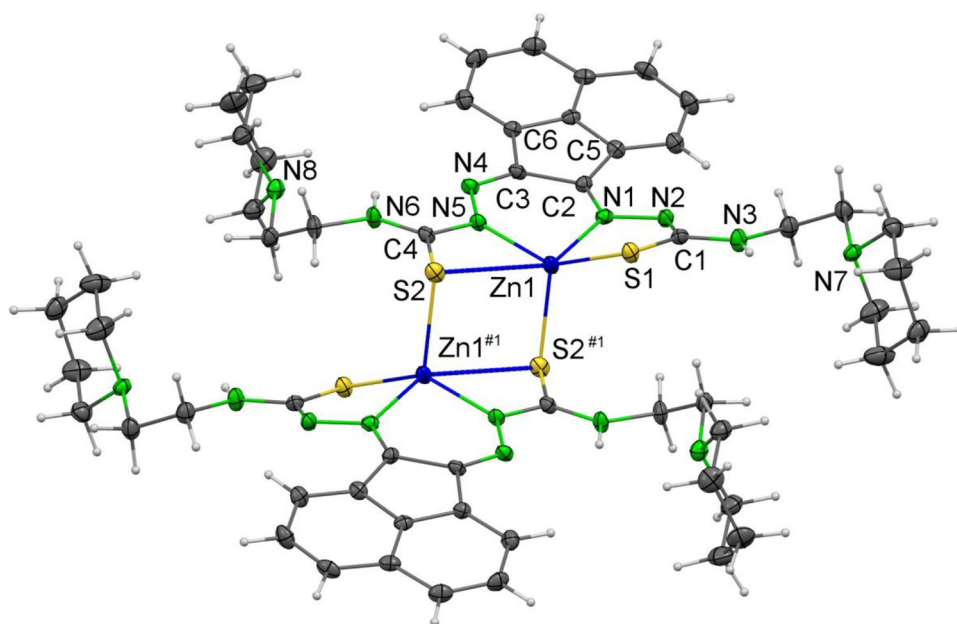

Fig. 3 ORTEP diagram of **ZnL^2** with thermal displacement ellipsoids at 40% probability level

of the other two chelate rings, Zn1–S1–C1–N2–N1 and Zn1–S2–C4–N5–N4, are 10.59(15)° and 28.50(17)°, respectively (see Table S3, SI). The **ZnL²** structure is stabilized by a significant network of intermolecular hydrogen bonds being the most relevant those formed between the water molecule at the axial position and the nitrogen atom of the morpholine moiety, O(3)–H(3AW)…N(7), with a bond length of 2.753(5) Å (Table S4 and Figure S7, SI).

In the structure of **ZnL³**, each unit lies close to an inversion center giving rise to a dimeric structure, thereby ensuring a distorted square-pyramidal coordination around each Zn atom through the bonding to the sulfur (S2#1) atom from the related symmetric unit at the axial position and to the S1, N1, N5, and S2 atoms on the basal plane (Fig. 4). The aromatic bis(thiosemicarbazone) ligand coordinates to the Zn atoms in a non-symmetrical fashion forming a system of four-, six-, and five-membered chelate rings. The dihedral angles formed by the l.s. plane of the aromatic acenaphthene moiety and the l.s. planes of the four-, six-, and five-membered chelate rings are 12.93(6)°, 1.68(7)°, and 35.22(4)°, respectively (see Table S3, SI). The value of 35.22(4)° observed for the dihedral angle involving the five-membered chelate ring is bigger than the corresponding values found in the **ZnL²** structure, certainly to minimize the steric constraints around the metal due to the greatest bulkiness and rigidity of **L³** [21, 22]. Most probably, this is the reason justifying the unusual asymmetric coordination observed for **L³**, which was reported previously for a related aromatic Zn(II) bis(thiosemicarbazonato) complex showing a bulky 1,4-diazabicyclo[2.2.2]octane ligand coordinated at the axial position [17].

ZnL² and **ZnL³** present bond angles and distances comparable (within the experimental error) to the values reported for other aliphatic or aromatic Zn^{II}BTSC complexes, with the C–S bond lengths (1.735Å–1.749Å) lying within the characteristic range for thiolate bonds [17, 18, 23–30]. The exceptions are the M–S and M–N bond lengths in the asymmetric **ZnL³** species, with a strong increase of the equatorial Zn–S2 bond involving the bridging sulfur atom (2.9679(11) Å) and a slight reduction in the Zn–N bonds [Zn–N1 2.068(3) Å and Zn–N5 1.982(3) Å]. Probably, this trend is due to the symmetry breakdown in the coordination geometry around the Zn atom and to the minimization of repulsive interactions within the dimer. For the bridging sulfur atom in **ZnL³**, the difference between its equatorial and axial Zn–S bonds (2.9679 Å and 2.4002 Å, respectively) is much larger than the one found for the bridging sulfurs in a related dimeric structure of a Zn(II) complex with a tridentate thiosemicarbazone (av. 2.555 Å and 2.410 Å for the equatorial and axial Zn–S bonds, respectively) [30, 31]. The most relevant intermolecular hydrogen bond interactions present in **ZnL³** are listed in Table S4 (SI).

All the Zn(II) complexes (**ZnL¹**–**ZnL⁴**) were analyzed by electrospray ionization mass spectrometry (ESI–MS) at room temperature, using dilute acetonitrile solutions of the pure compounds. The obtained ESI–MS spectra in the positive mode showed peaks and isotopic patterns consistent with the presence of [M + H]⁺ or [M + Na]⁺ ions corresponding to monomeric species (see experimental section). We should emphasize that this behavior was also observed for **ZnL³** despite the fact that it crystallized in the solid state as a dimeric compound. The positive ESI–MS spectrum of **ZnL³** showed a prominent [M + H]⁺ peak at $m/z = 613.2$

with a splitting pattern superimposable to the one calculated for monoprotonated **ZnL³** monomers (ESI, Figure S13). The peak due to monoprotonated dimer adducts at *m/z* 1229.38 or the peak at *m/z* 615.19 attributable to the double protonation of the dimeric **ZnL³** species was not present in the experimental spectrum.

UV/Vis and fluorescence spectroscopy

As mentioned before, other authors showed that BTSC Zn(II) complexes containing an aromatic backbone, namely, the symmetric **ZnNqTSM**, are more efficient fluorophores than **ZnATSM** and related aliphatic complexes [17]. Therefore, we expected the aromatic BTSC Zn(II) complexes described in this work to present fluorescence properties suitable for live-cell imaging studies. For a reliable interpretation of the live-cell imaging results (see below), we started by characterizing the complexes by UV/Vis absorption and fluorescence spectroscopies.

As shown in Fig. 5, the absorption spectra of **ZnNqTS-Masym**, **ZnL³**, and **ZnL⁴** solutions in DMSO are almost superimposable, showing a strong absorption band centered at around 360 nm and a set of weaker bands between 410 nm and 510 nm. The shape of these spectra and the energy of their bands are very similar to those described previously for symmetric **ZnNqTSM** [18]. The high-energy bands can be assigned to the transfer of electron density from metal-based orbitals to the naphthyl moieties of the ligands. The bands at lower energy are probably associated with $\pi \rightarrow \pi^*$ and $n \rightarrow \pi^*$ [HOMO–LUMO (type)] transitions involving the sulfur lone pair and orbitals associated with the diimine bonds and naphthyl backbone. Complexes **ZnL¹** and **ZnL²** show absorption bands at ca. 315 and 437 nm.

The three aromatic Zn(II) complexes, **ZnNqTSM**^asym, **ZnL³**, and **ZnL⁴**, emit fluorescence in DMSO when irradiated at 370 nm that corresponds approximately to λ_{max} of the most intense absorption band, giving rise to fluorescence spectra presenting emission bands centered at 563 nm (Fig. 5). The same bands also appear by irradiating at 445 nm, although less intense (Figure S16, SI). Complexes **ZnL¹** and **ZnL²** show very weak fluorescence emission (see SI).

Fig. 5 UV–visible absorption spectra (top) and fluorescence emission spectra (λ_{exc} 370 nm, r.t., bottom) of the zinc(II) complexes in DMSO (15 μM)
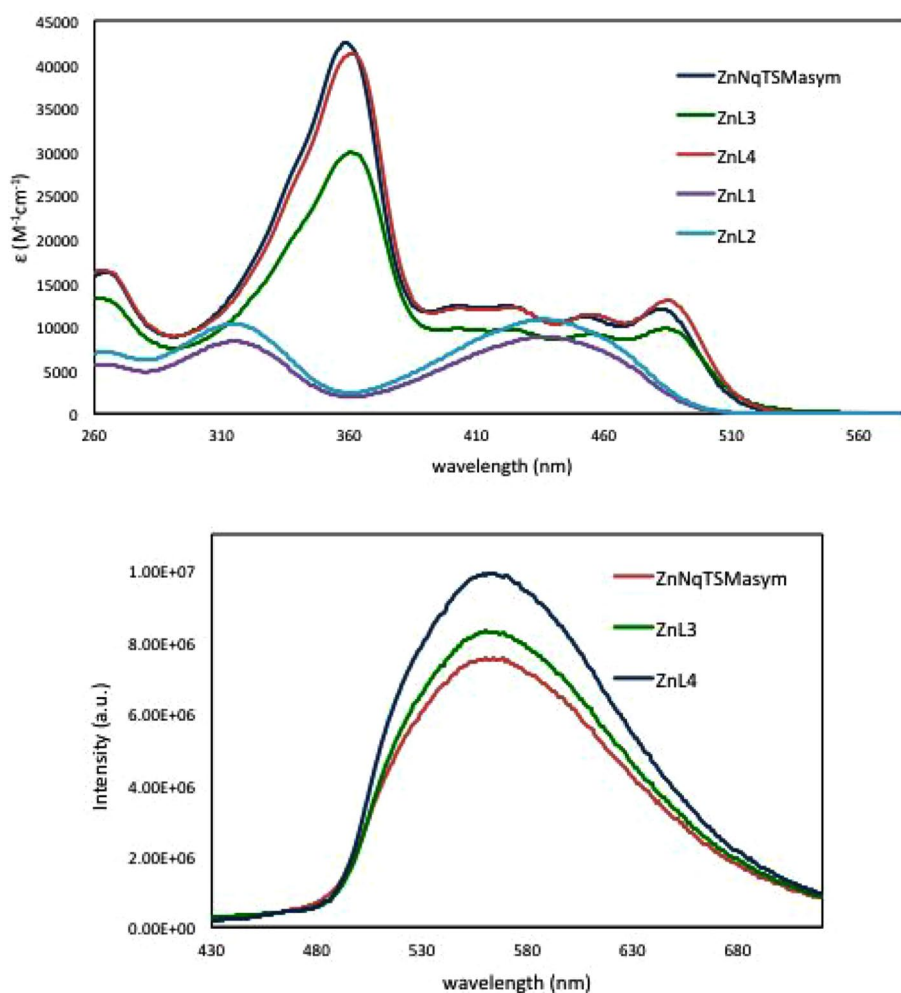
Table 1 Photophysical properties of the Zn(II) complexes in DMSO solution at room temperature

	λ_{abs}/nm (ε/M^{-1}cm^{-1})	λ_{em}/nm	τ/ns	Φ^a
ZnNqTSM^{asym}	359 (4.24×10^4)	560	0.14	0.060
	402 (1.23×10^4)			
	424 (1.23×10^4)			
	454 (1.10×10^4)			
	483 (1.20×10^4)			
ZnL^1	314 (8.25×10^3)	545	n.d	n.d
	438 (8.81×10^3)			
ZnL^2	315 (1.03×10^4)	545	n.d	n.d
	437 (1.08×10^4)			
ZnL^3	361 (2.99×10^4)	560	0.14	0.074
	404 (9.71×10^3)			
	425 (9.60×10^3)			
	456 (9.11×10^3)			
	485 (9.75×10^3)			
ZnL^4	361 (4.12×10^4)	561	0.11	0.074
	403 (1.21×10^4)			
	424 (1.22×10^4)			
	453 (1.14×10^4)			
	486 (1.29×10^4)			

^{a}Measured by comparison with the emission of quinine sulphate in 0.5 M H$_2$SO$_4$ ($\Phi=0.55$) [32, 33]

The quantum yields (Φ) in DMSO were estimated by the relative method, using quinine sulphate as the reference (Table 1) [32, 33]. The values obtained are in good agreement with results previously reported for similar compounds, namely, symmetrical **ZnNqTSM** [18]. Time-resolved fluorescence enabled the determination of the average lifetime

(τ) for the complexes (Table 1). In summary, the three aromatic BTSC Zn(II) complexes show fluorescence emission around 563 nm, with quantum yields between 0.060 and 0.074 and average lifetimes in the range 0.11–0.14 ns, possessing, therefore, favorable features for fluorescence microscopy studies.

Biological evaluation

Cytotoxic activity in human tumoral cell lines

To have insight on the antitumoral properties of the new Zn^{II}BTSC complexes, their cytotoxic activities were studied using a panel of human cancer cell lines, and compared with those of the respective chelators and **ZnATSM**. For comparative purposes, all the compounds were also tested in the human non-tumoral HEK293 cell line. For these assays, cells were incubated with increasing concentrations of the compounds for 48 h at 37 °C, and the cellular viability was evaluated by the MTT assay. The inhibition of growth (%) was calculated and the IC$_{50}$ values (i.e., concentration which reduces the growth by 50%) were determined and are presented in Table 2.

For the aliphatic BTSCs, there is a clear effect of metal complexation on their cytotoxic profile in most of the cell lines studied. This trend is in agreement with the results reported in the literature for other Zn(II) complexes of thiosemicarbazone-based ligands, with the complexes displaying in general a significantly greater cytotoxicity than the corresponding thiosemicarbazones [3].

Nevertheless, the presence of the pendant cyclic amine groups in the aliphatic BTSC has a negative effect on the antitumoral activity of the respective Zn(II) complexes for

Table 2 IC$_{50}$ (µM) values of the Zn^{II}BTSC complexes and respective ligands, as determined by the MTT assay after 48 h of incubation of the compounds at 37 °C with human non-tumoral HEK293 and tumoral cell lines: ovarian—A2780 and A2780cisR, breast—MCF7, cervical—HeLa, and prostate—PC3 and LNCap

	IC$_{50}$ (µM)						
	A2780	A2780cisR	MCF7	HeLa	PC3	LNCap	HEK293
ATSM	60.8 ± 10.7	>200	20.6 ± 4.9	100.1 ± 27.9	112.4 ± 40.6	14.65 ± 4.62	25.9 ± 3.99
H$_2$L^1	>200	>200	59.5 ± 22.7	130.4 ± 70.8	117.0 ± 39.9	18.62 ± 4.55	108.4 ± 44.7
H$_2$L^2	>200	>200	>200	106.7 ± 20.5	145.0 ± 143.8	54.7 ± 21.3	161.0 ± 61.0
H$_2$NqTSM	36.9 ± 11.0	35.5 ± 9.23	4.29 ± 0.88	17.6 ± 7.8	59.4 ± 24.7	13.4 ± 4.3	1.44 ± 0.46
H$_2$L^3	1.68 ± 0.37	3.50 ± 1.41	1.22 ± 0.28	4.92 ± 0.70	7.81 ± 2.34	6.69 ± 2.68	0.67 ± 0.15
H$_2$L^4	3.00 ± 0.42	12.3 ± 2.07	5.68 ± 1.59	5.55 ± 0.86	16.1 ± 4.3	6.38 ± 1.43	1.87 ± 0.42
ZnATSM	6.62 ± 3.07	8.49 ± 4.81	8.90 ± 4.07	24.4 ± 7.1	10.7 ± 2.8	9.33 ± 2.96	2.78 ± 1.49
ZnL^1	50.5 ± 32.1	33.5 ± 12.8	85.6 ± 57.3	79.9 ± 35.3	47.6 ± 18.6	47.3 ± 35.0	31.8 ± 13.5
ZnL^2	66.8 ± 43.9	57.8 ± 25.0	$58.8\pm20,1$	89.5 ± 18.8	59.7 ± 26.4	46.5 ± 14.8	42.4 ± 15.0
ZnNqTSM^{asym}	2.53 ± 0.78	4.27 ± 1.36	4.70 ± 1.12	11.0 ± 2.5	5.79 ± 1.95	3.49 ± 0.43	0.93 ± 0.17
ZnL^3	2.21 ± 0.76	4.94 ± 1.91	5.26 ± 1.80	4.15 ± 1.00	4.78 ± 1.43	3.16 ± 1.73	2.98 ± 0.89
ZnL^4	2.51 ± 0.46	11.9 ± 4.5	20.6 ± 7.3	7.08 ± 1.97	9.35 ± 4.93	8.46 ± 2.72	3.97 ± 0.91

all the cell lines studied. In fact, ZnL^1 and ZnL^2 present IC_{50} values that are roughly 4–10 times higher than those exhibited by the parental ZnATSM. For instance, in A2780 cells, IC_{50} values are 50.5 and 66.8 μM for ZnL^1 and ZnL^2, respectively, and 6.62 μM for $ZnATSM$. In contrast, and as reported previously by us [14], the congener Cu(II) complexes (CuL^1 and CuL^2), carrying the same pendant cyclic amine rings (piperidine or morpholine, respectively), exhibited lower IC_{50} values than $CuATSM$.

In general, each aliphatic and aromatic complex shares rather similar anti-proliferative properties in the tumoral cell lines when compared with the non-tumoral cell line. However, regarding the complexes containing the aromatic naphthyl core and pendant cyclic amine groups, ZnL^3 and ZnL^4, they presented a much stronger anti-proliferative action than their aliphatic counterparts, ZnL^1 and ZnL^2. For example, IC_{50} values of 2.21 ± 0.76 and 2.51 ± 0.46 μM were obtained in A2780 cells for ZnL^3 and ZnL^4, respectively, while 20–25 times higher IC_{50} values were obtained for ZnL^1 and ZnL^2 (50.5 ± 32.1 and 66.8 ± 43.9 μM, respectively). Complex $ZnNqTSM^{asym}$ also showed higher cytotoxic activity (ca. twofold lower IC_{50} values) than $ZnATSM$ (A2780: 2.53 ± 0.78 vs 6.62 ± 3.07 μM; A2780cisR: 4.27 ± 1.36 vs 8.49 ± 4.81 μM; MCF-7: 4.70 ± 1.12 vs 8.90 ± 4.07 μM). The same trend was previously reported for the cytotoxic activities of symmetrical $ZnNqTSM$ derivatives and related aliphatic congeners [17, 18].

Altogether, these data corroborate the crucial influence of the aromatic backbone on the biological performance of BTSC Zn(II) complexes. This influence was also noticed in the biological activity of the respective free ligands, as the new aromatic BTSCs (H_2L^3 and H_2L^4) are much more cytotoxic than the aliphatic counterparts (H_2L^1 and H_2L^2). Moreover, the aromatic BTSCs and the respective Zn(II) complexes showed similar IC_{50} values in almost all tested cell lines. The influence of the piperidine and morpholine pendant arms in the cytotoxic activity of the compounds is less striking than that of the aromatic vs aliphatic backbone. However, as a general trend, it is evident that the piperidine groups confer a higher cytotoxicity to the compounds when compared with the morpholine congeners, both for the aromatic and aliphatic systems. This trend is well illustrated by the highest cytotoxicity values exhibited by ZnL^3 in different human tumoral cell lines, among all the complexes carrying pendant cyclic amines.

Live-cell fluorescence imaging

Taking advantage of the intrinsic fluorescence of the aromatic BTSC Zn(II) complexes ($ZnNqTSM^{asym}$, ZnL^3, and ZnL^4), a live-cell fluorescence microscopy assay was performed to assess their ability to enter human tumoral cells, visualize their subcellular localization and eventual

accumulation in given organelles. MCF7 cells were observed in the fluorescence microscope for 1 h after adding Zn(II) complexes or DMSO while monitoring the fluorescence co-localizing with the cells. Figure 6a shows representative microscopy images of MCF7 cells incubated with 20 μM of each complex. A control experiment, where cells were incubated with DMSO, was used to assess background fluorescence and cellular autofluorescence. Figure 6b presents a quantitative kinetic analysis of the compounds accumulation.

Overall, ZnL^3 was the complex that presented the fastest uptake, measured by the detected intracellular fluorescence that increased steadily for ~ 30 min. ZnL^4 and $ZnNqTS-M^{asym}$ demonstrated a slower and moderate cell uptake (~ 2,5 times lower than ZnL^3), reaching similar levels of fluorescence at 60 min of incubation.

Importantly, when cells were incubated with 10 μM of ZnL^3 (corresponding to half the concentration represented in Fig. 6), the intracellular fluorescence detected was still higher than for the rest of the complexes at 20 μM (data not shown). The positive influence of the pendant cyclic amine groups in the kinetics of cell uptake, particularly in the case of the piperidine ring, is consistent with the behavior that we found previously for Cu(II) complexes (CuL^1 and CuL^2) with aliphatic BTSCs [14].

After 30 min of live-cell imaging and particularly in the case of cells incubated with ZnL^3, cells started presenting signs of membrane blebbing. This suggests the occurrence of apoptosis, which might lead to membrane permeabilization and consequent loss of the intracellular fluorescence due to ZnL^3. This effect is most likely due to the cytotoxic properties of the complex, as the excitation was short and performed in mild conditions and the nuclear stain was also used at a non-toxic concentration. In addition, this effect was not observed in the DMSO control. Considering that the evaluated Zn(II) complexes present similar spectral characteristics (see Fig. 5 and Table 1), the differences observed for the intracellular fluorescence are most likely the result of different cellular uptake.

The observed intracellular distribution of the fluorescence, and hence of the compounds, was diffuse in the cytoplasm without accumulation in the nucleus. As mentioned in the introduction, we have hypothesized that the presence of the protonable cyclic amines could provide the BTSC Zn(II) complexes with lysosomotropic properties, as described in the literature for other compounds [15, 16]. Therefore, we next evaluated if the presence of the piperidine ring could promote the lysosomal entrapping of ZnL^3. The lysosomal-specific fluorescent probe, lysotracker red DND-99, was used in co-localization experiments in live cells incubated with ZnL^3 and $ZnNqTSM^{asym}$. In accordance with the previous experiment, a stronger green fluorescence was detected in cells incubated with ZnL^3 compared with cells incubated with

Fig. 6 Cell uptake kinetics of the aromatic BTSC Zn(II) complexes in MCF7 cells, as measured by fluorescence microscopy. **a** Representative images of MCF7 cells incubated with the compounds for 30 min. Images correspond to the intrinsic compound fluorescence, bright field (overall cell morphology), Hoechst 33342 fluorescence (cell nuclei) and a merged image, with the compound fluorescence in green, nuclei in cyan and brightfield in gray. Scale bar = 50 μm. **b** Quantification of compounds intrinsic fluorescence co-localizing with cells during the live-cell kinetic assay. Increasing measurements indicate cellular accumulation of the compounds. Values are average ± standard deviation
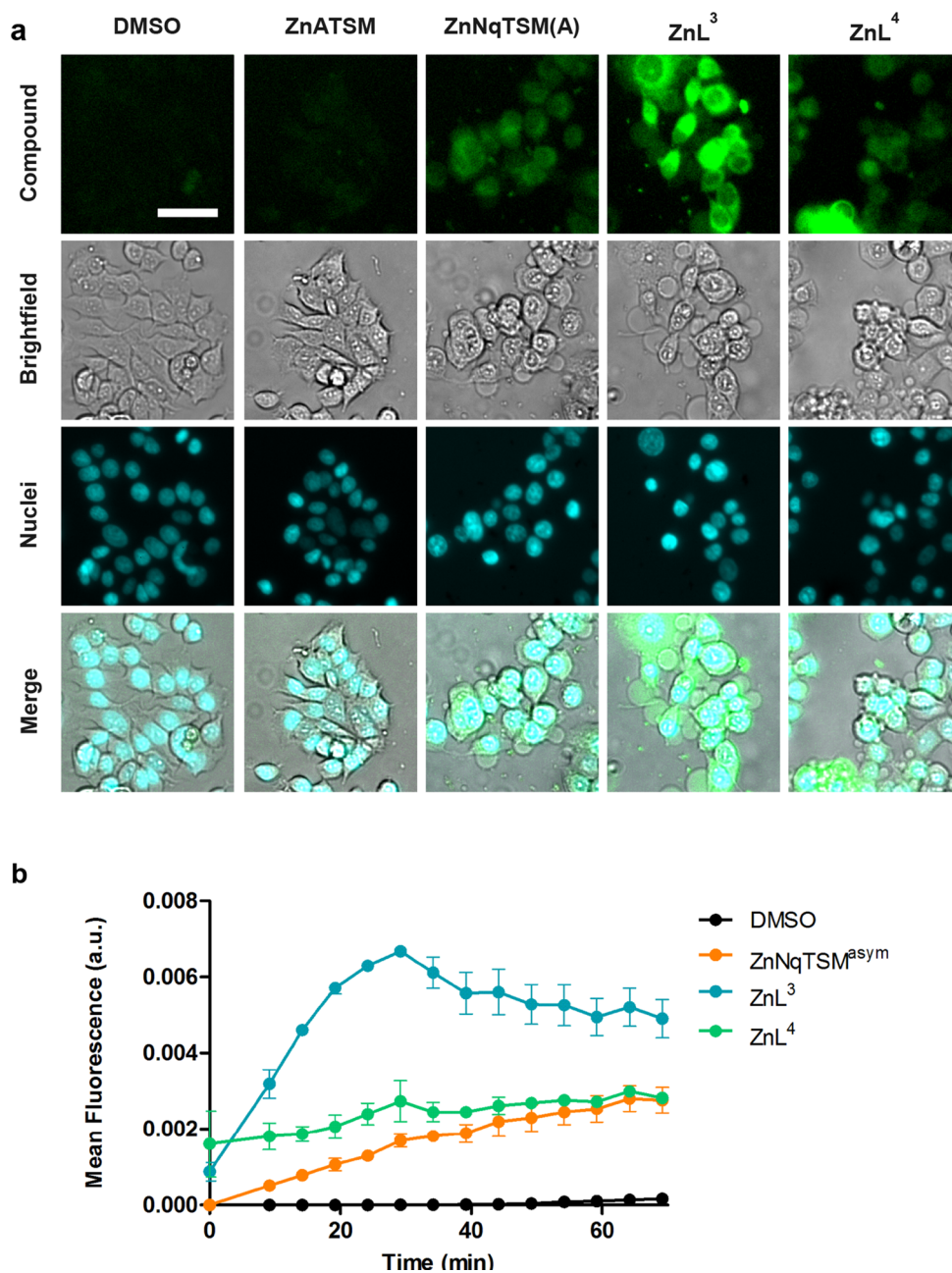
ZnNqTSM^{asym}. Some of that intracellular fluorescence, particularly for **ZnL^3**, was strongly co-localized with the lysosomal marker, indicating the lysosomal entrapping of this aromatic Zn complex. When cells were incubated with the model **ZnNqTSM^{asym}** and lysotracker a less intense co-staining was detected (Fig. 7). These results suggest that there is an influence of the piperidine arm in the subcellular distribution of the Zn complexes, namely, in their lysosomal trapping.

Cellular uptake studies by ICP-MS

Searching to correlate the cytotoxic activity of the aliphatic and aromatic BTSC Zn(II) complexes with their ability to enter the cells, the quantitative assessment of the uptake of the compounds in MCF7 cells was performed by determining their total Zn content using ICP-MS. In this assay, the amount of total Zn in cells incubated with the compounds was determined, and compared with the total

Fig. 7 Co-localization of aromatic BTSC Zn(II) complexes with the lysosomes in MCF7 cells. MCF7 cells were incubated with Lysotracker, as well as **ZnL³** (**a**) or **ZnNqTSM^asym** (**b**) for 30 min in a live-cell fluorescence microscopy experiment. Scale bar: 50 μm
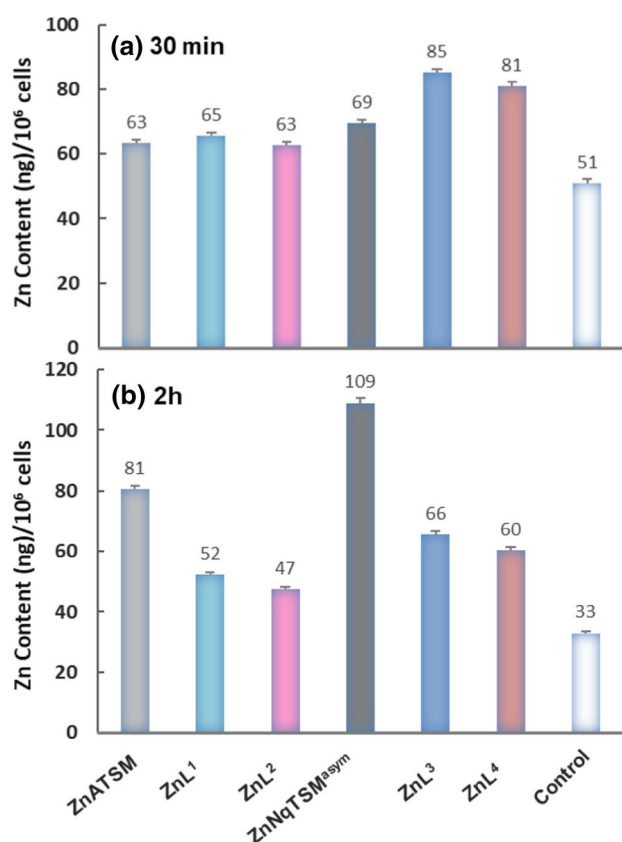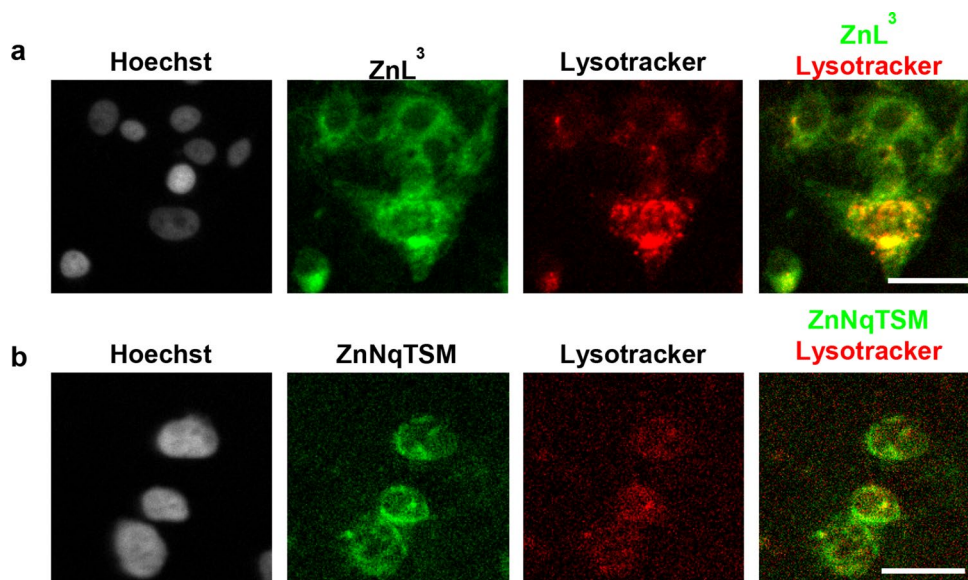

Fig. 8 Uptake of the BTSC Zn(II) complexes in MCF7 cells. Cells were incubated with the tested compounds (10 μM) or with DMSO as control for 30 min (**a**) and 2 h (**b**) at 37 °C. Thereafter, the concentration of Zn in the cellular pellet was determined by ICP-MS and data expressed as metal (Zn) content per million cells

Zn in same number of cells incubated only with growth media, taking into consideration that Zn is an endogenous element involved in numerous processes of cellular metabolism [34].

Cells were incubated with **ZnATSM**, **ZnNqTSM^asym**, and **ZnL^{1−4}** at 10 μM for 30 min and 2 h. After appropriate processing, the cellular pellets were analyzed by ICP-MS, as detailed in the experimental section. As shown in Fig. 8, the incubation of MCF7 cells with the compounds led to an increase of the intracellular Zn concentration in comparison with the control, showing that all the Zn(II) complexes have the ability to accumulate in this tumoral cell line model. For both incubation times, the aromatic BTSC Zn(II) complexes showed higher cellular uptake than the aliphatic counterparts with the same N-terminal substituents, i.e., **ZnNqTSM^asym > ZnATSM**, **ZnL³ > ZnL¹**, and **ZnL⁴ > ZnL²**.

The determination of the zinc cellular content by ICP-MS at 30 min of incubation showed that **ZnL³** presented the highest uptake (Fig. 8a). This result is in agreement with the live-cell imaging studies that showed a faster uptake kinetics for **ZnL³** in comparison with **ZnNqTSM^asym** (see Fig. 6). In contrast, after 2 h of incubation, **ZnNqTSM^asym** exhibited higher total Zn uptake than **ZnL³**. This trend can be accounted by the steadily increasing uptake observed for **ZnNqTSM^asym** and the faster cellular release found for **ZnL³**, up to 60 min, which was the final timepoint of the live-cell imaging studies. As mentioned above, after 30 min cells incubated with **ZnL³** presented signs suggestive of apoptosis that could lead to loss of the intracellularly accumulated **ZnL³**.

As a general trend, the cytotoxic activity of the complexes in the MCF7 cell line followed the trend observed for their cellular uptake. Furthermore, the presence of the aromatic naphthalene backbone appears to have an important role in

the cellular uptake of the Zn(II) complexes and in their cytotoxic activity.

Effects on lysosomal integrity and ROS generation

Among the new compounds carrying cyclic amine groups, **ZnL³** and the corresponding free ligand, **H₂L³**, showed the greatest cytotoxic activity; moreover, **ZnL³** showed the fastest uptake kinetics and highest cellular uptake, as well as lysosomal localization, according to the results of live-cell imaging experiments and ICP-MS measurements. Thus, this complex and respective ligand were chosen to proceed with additional in vitro studies aiming to obtain some insight on the mechanism of action of the compounds. As mentioned in the introduction, thiosemicarbazones and their Zn(II) complexes have shown multiple mechanisms of action, and it has been demonstrated in several instances that the lysosomal membrane permeabilization (LMP) gives an important contribution to their biological effects [3, 9–13]. Therefore, next, we examined whether **ZnL³** and **H₂L³** could also induce LMP.

The studies were performed using acridine orange (AO) as a lysosomotropic fluorophore, which when concentrated in lysosomes emits granular red fluorescence, whereas in the cytosol or nucleus emits diffuse green fluorescence. Reduction in granular red fluorescence combined with increased diffuse cytosolic green fluorescence typically indicates relocation of AO from the lysosomes to the cytosol, following changes in lysosomal membrane permeability. To examine the ability of **ZnL³** and respective ligand to affect LMP, MCF7 cells were incubated with the compounds for 1 h at 37 °C, following a 15 min pre-incubation with AO. Next, the cells were imaged by fluorescence microscopy and the results obtained are presented in Fig. 9.

Control MCF7 cells, treated only with AO, showed granular red fluorescence consistent with the concentration of AO in lysosomes (Fig. 9b). Treatment of the cells with **H₂L³** and **ZnL³** resulted in increased cytosolic green fluorescence and reduced lysosomal red fluorescence (Fig. 9c, d). Consequently, a significant ($p < 0.01$) reduction of ca. 40% was observed for the red:green fluorescence ratio. This effect is due to the relocation of AO from the lysosomes to the cytosol, indicating that both **H₂L³** and **ZnL³** were able to induce LMP.

It is also important to notice that the LMP activity observed for **H₂L³** and **ZnL³** does not strictly depend on their lysosomal localization, but also might reflect their ability to mediate ROS generation intracellularly. Thus, this effect was evaluated in MCF7 cells using the redox-sensitive probe 2′,7′-dichlorodihydrofluorescein diacetate (H₂DCF-DA), which is oxidized by ROS to the highly fluorescent product 2′,7′-dichlorofluorescein (DCF) [35]. To assess the generation of ROS, MCF7 cells were treated with **H₂L³** and **ZnL³** (2, 10, 20 μM) for 30 min and then incubated with 1 μM H₂DCF-DA for a further 30 min. As shown in Fig. 10, cells incubated with the compounds were imaged by fluorescence microscopy, in parallel with a positive control consisting on cells exposed to H₂DCF-DA and H₂O₂ and a negative control consisting on cells treated uniquely with DMSO vehicle.

The positive control, H₂O₂, led to a substantial increase (~2.5-fold of negative control) in DCF fluorescence. The

Fig. 9 Evaluation of LMP induced by **ZnL³** and **H₂L³** using the AO lysosomal integrity assay in MCF7 cells. Cells were pre-incubated with AO (5 μg/mL) for 15 min, followed by an 1 h incubation with the tested compounds (10 μM). **a** Quantification of the red:green fluorescence ratio (expressed data are presented as average ± standard deviation normalized to the AO control). **b–d** Images of cells incubated with AO only (control) and treated with **H₂L³** and **ZnL³**, respectively
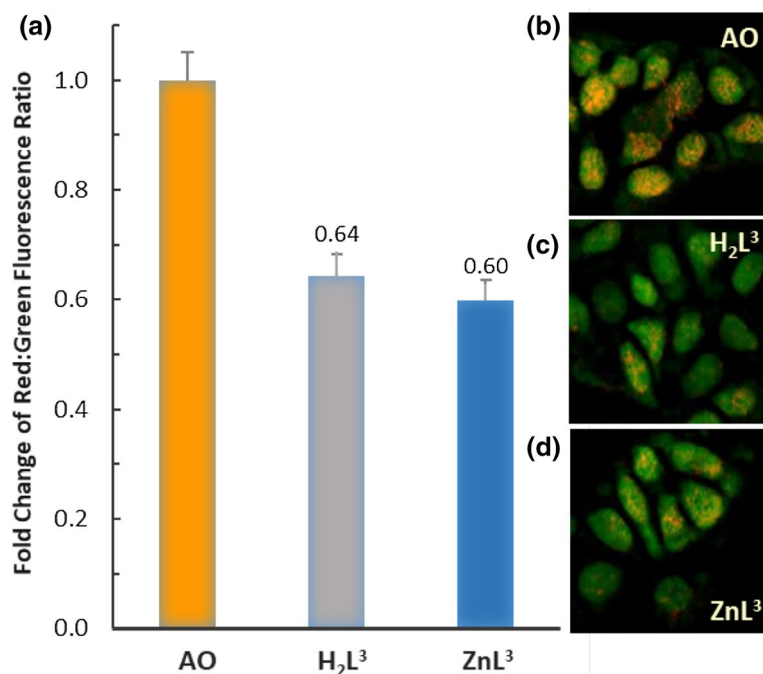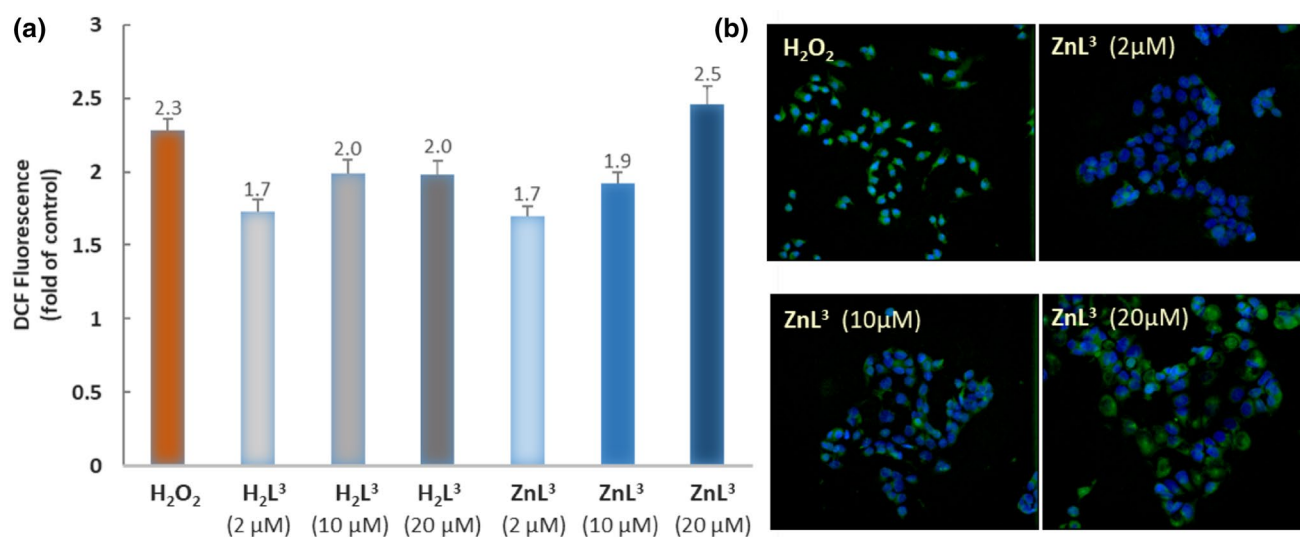
Fig. 10 Redox activity of **ZnL³** and respective ligand **H₂L³** (2, 10 and 20 µM, 30 min) in MCF7 cells incubated with H₂DCF-DA (1 µM, 30 min). H₂O₂ was included as a positive control. **a** Quantification of DCF fluorescence normalized to the negative control (H₂DCF-DA alone) presented as average ± standard deviation. **b** Representative images of DCF fluorescence in cells incubated with H₂O₂ and treated with different concentrations of **ZnL³**

treatment of cells with increasing concentrations of **ZnL³** resulted in the incremental generation of ROS, with the highest concentration (20 µM) inducing ROS production to levels 2.5 times higher than the negative control and even slightly superior to the positive control.

In agreement with the cytotoxic and the LMP effects observed for both compounds, similar values of DCF fluorescence (ROS production) were detected for **H₂L³** and **ZnL³**, in particular for the lowest concentrations. These results indicate that the LMP effect induced by **H₂L³** and **ZnL³** is probably due to ROS production. ROS can destabilize the lysosomal membrane by causing lipid peroxidation and damaging lysosomal membrane proteins [36]. However, other processes can account for the cytotoxicity of the compounds, since a variety of cellular structures and pathways can be affected by ROS generation. Moreover, it has been recently demonstrated that the mechanism of action of Zn(II) complexes with di-2-pyridylketone (DpT) and 2-acetylpyridine (ApT) thiosemicarbazone chelators involves sequestration within the lysosomes and trans-metalation with intralysosomal Cu²⁺ to produce redox active complexes that induce LMP-mediated cytotoxicity by ROS [3]. The similar IC₅₀ values exhibited by **H₂L³** and **ZnL³** in the tested cell lines, as well as the similar ability to induce LMP and produce ROS, point out for the involvement of the same type of mechanisms with a possible contribution of trans-metalation with copper ions. Although justifying further investigation, we have considered that this aspect was out of the scope of the present contribution.

Conclusions

New BTSC Zn(II) complexes bearing piperidine and morpholine pendant arms, based on aliphatic and aromatic scaffolds were synthesized and thoroughly characterized. In the aliphatic derivatives, **ZnL¹** and **ZnL²**, the BTSC chelators present symmetrical N₂S₂ coordination mode. The aromatic counterparts, **ZnL³** and **ZnL⁴**, formed asymmetric Zn(II) complexes, which most probably reflected the (*E,Z*) conformation of the **H₂L³** and **H₂L⁴** compounds, that are pre-organized to coordinate the metal center through one inner and one outer imine nitrogen atoms.

The aromatic complexes showed fluorescence properties, which were characterized and allowed live-cell imaging studies. The biological evaluation of the complexes demonstrated that **ZnL³** and **ZnL⁴** showed much stronger anti-proliferative action than the aliphatic **ZnL¹** and **ZnL²**, which could be correlated with their higher cell uptake as demonstrated by ICP-MS. Complex **ZnL³** presented the fastest cell uptake kinetics in tumoral cells, showed lysosomal entrapping and was able to generate intracellular ROS, which induced lysosomal membrane damage. Altogether these data indicate that the presence of the pendant cyclic amines might influence the cell uptake mechanisms of BTSC Zn(II) complexes, most likely endowing them with lysosomotropic properties. However, more detailed mechanistic studies are needed to fully elucidate the effect of the pendant cyclic amines in the cell uptake kinetics of

this class of Zn(II) complexes and on their intracellular localization.

Experimental section

Materials and methods

All chemicals were p.a. grade and were used without purification unless stated otherwise. **H₂L¹**, **H₂L²**, **H₂NqTSM** and **ZnATSM** were synthesized as described in the literature [14, 18, 19]. The chemical reactions were followed by thin-layer chromatography (TLC). TLC was performed on pre-coated silica plates 60 F_{254} (Merck). Visualization of the plates was carried out using UV light (254 nm) and/or iodine chamber. Gravity column chromatography was carried out on silica gel (Merck, 70–230 mesh).

Elemental analyses (CHN) were recorded on an EA 110CE automated instrument. Zn determinations were performed by inductively coupled plasma mass spectrometry (ICP-MS) using a quadrupole mass filter ICP-MS, the ELAN DRC-e from PerkinElmer Sciex (Axial Field Technology). Electrospray ionization mass spectrometry (ESI–MS) was performed on a QITMS instrument in positive and negative ionization mode. ¹H and ¹³C NMR spectra were recorded on a Varian Unity 300 MHz or 400 MHz spectrometer at the frequencies of 300 or 400 MHz (¹H) and 75 or 100 MHz (¹³C), respectively. ¹H and ¹³C chemical shifts (δ) are reported in ppm relative to residual solvent signals (DMSO-d_6: 2.50 ppm for ¹H NMR and 39.52 ppm for ¹³C NMR; C₃OD: 3.31 ppm for ¹H NMR and 49.00 ppm for ¹³C NMR). The compounds were characterized by electrospray ionization mass spectrometry (ESI–MS) using a Bruker model Esquire 3000 plus. The spectra were acquired at room temperature, using acetonitrile diluted solutions of the pure compounds. IR spectra were recorded in KBr pellets on a Bruker Tensor 27 spectrometer. UV–visible absorption spectra were recorded on Perkin Elmer Lambda 35 UV–Vis spectrophotometer with 1 cm quartz cuvettes. Steady-state fluorescence measurements were carried out on a SPEX® Fluorolog spectrofluorimeter (Horiba Jobin–Yvon) in an FL3–11 configuration, equipped with a Xenon lamp and in a 1 cm quartz cuvette. The instrumental response was corrected by means of a correction function provided by the manufacturer. Fluorescence average lifetimes were determined using a 372 nm HORIBA Jobin–Yvon NanoLED as light source.

General procedure for the synthesis of aromatic BTSCs

A solution of 4-substituted-3-thiosemicarbazide (3 mmol) and acenaphthenequinone (1 mmol) in ethanol (2 mL) and 2 M HCl (2 mL) was refluxed overnight. Then, triethylamine was added until basic pH. The aqueous phase was diluted with water (50 mL) and extracted with dichloromethane (2 × 50 mL). The organic phase was dried over Na₂SO₄, filtered, concentrated under vacuum and then submitted to column chromatography on silica gel (CH₂Cl₂/MeOH/NEt₃ 1:0.05:0.01) to give the desired BTSC as a reddish solid, which was further washed with dichloromethane and n-hexane.

bis[4-N-(2´-(piperidine-1-yl)ethyl)-3-thiosemicarbazone] acenaphthenequinone (H₂L³)—yield = 53%; R_f (DCM:MeOH:TFA 1:0.1:0.01) = 0.3; ¹H NMR (DMSO-d_6, 300 MHz) δ 1.46 (m, 4H), 1.58 (m, 8H), 2.65 (m, 8H), 2.76 (m, 4H), 3.78 (m, 4H), 7.82 (m, 2H), 8.03 (m, 2H), 8.11 (m, 1H), 8.33 (m, 1H), 8.55 (br s, 1H, NH), 9.01 (br s, 1H, NH), 11.09 (br s, 1H, NH), 12.86 (s, 1H, NH); ¹³C NMR (DMSO-d_6, 75 MHz) δ 24.46, 24.78, 25.98, 26.45, 41.88, 42.26, 54.73, 54.80, 57.39, 57.80, 118.73, 125.31, 127.59, 129.22, 130.92, 133.62, 133.94, 136.60 (C=N), 178.33 (NHC=S); ES⁺ MS C₂₈H₃₈N₈S₂ (550.27) m/z 551.5 [M + H]⁺; Anal. calcd. for C₂₈H₃₈N₈S₂.H₂O: C 59.12, H 7.09, N 19.74; found C 59.08, H 7.39, N 19.80. IR (KBr, ν/cm⁻¹): 3287 (w), 2934 (s, N–H), 2083 (w), 1533 (vs, C=N), 1476 (vs, C=N), 1183 (s, thioamide), 1112 (s, N–N), 822, 772. (vs, very strong; s, strong; m, medium; w, weak; sh, sharp). UV–Vis (DMSO) λ/nm (ε/M⁻¹cm⁻¹): 335 (1.95 × 10⁴); 438 (8.55 × 10³); 464 (8.34 × 10³); 490 (5.73 × 10³).

bis[4-N-(3´-morpholinoethyl)-3-thiosemicarbazone] acenaphthenequinone (H²L⁴)—yield = 65%; R_f (DCM:MeOH:TFA 1:0.1:0.01) = 0.3; ¹H NMR (DMSO-d_6, 300 MHz) δ ~ 2.50 (8H under DMSO-d_6 signal, confirmed by COSY), 2.62 (m, 4H), 3.59 (m, 8H), 3.77 (m, 4H), 7.80 (overlapped triplets, ³J = 8.0 Hz, 2H), 8.04 (m, 2H), 8.14 (d, ³J = 8.3 Hz, 1H), 8.24 (d, ³J = 7.2 Hz, 1H), 8.72 (br t, 1H, NH), 9.06 (br t, 1H, NH), 11.30 (br s, 1H, NH), 12.62 (s, 1H, NH); ¹³C NMR (DMSO-d_6, 75 MHz) δ 40.86, 41.41, 53.27, 56.45, 66.30, 118.23, 124.68, 126.89, 127.81, 128.29, 128.59, 128.97, 130.03, 132.78, 136.14, 138.04, 142.23, 146.44. ES⁺ MS C₂₆H₃₄N₈O₂S₂ (554.2) m/z: 555.3 [M + H]⁺; Anal. calcd. for C₂₆H₃₄N₈O₂S₂.H₂O: C 54.52, H 6.34, N 19.56; found C 54.36, H 6.46, N 19.62. IR (KBr, ν/cm⁻¹): 3443 (s, NH), 3315 (s, NH), 1536 (vs, C=N), 1478 (vs, C=N), 1298 (s, thioamide), 1133 (s, N–N), 976, 768. UV–Vis (DMSO) λ/nm (ε/M⁻¹cm⁻¹): 334 (2.89 × 10⁴); 462 (1.53 × 10⁴); 488 (1.38 × 10⁴); 604 (4.67 × 10²).

General procedure for the synthesis of BTSC zinc(II) complexes

To a suspension of the BTSC ligand (**H₂NqTSM**, **H₂L¹–H₂L⁴**; 0.2–0.4 mmol) in methanol (5 mL) was added one equivalent of zinc acetate dihydrate and the mixture was stirred overnight at RT (**ZnL¹** and **ZnL²**) or at reflux

(**ZnNqTSM^{asym}**, **ZnL^3** and **ZnL^4**). The yellow/orange precipitates of **ZnNqTSM^{asym}**, **ZnL^1** and **ZnL^2** were recovered by filtration and washed with 20 mL of methanol and 3×10 mL of diethyl ether. For **ZnL^3** the reaction mixture was dried in vacuum and the yellow–orange complex was obtained in a pure form after recrystallization in a mixture of dichloromethane and diethyl ether. **ZnL^4** precipitated from the reaction mixture and was recovered by filtration as a yellow–orange solid.

Zinc bis(4-*N*-methyl-3-thiosemicarbazone) acenaphthenequinone (ZnNqTSM^{asym})—yield = 80%; ^{1}H NMR (DMSO-d_6, 300 MHz) δ 3.09 (d, 3H, Me), 3.12 (d, 3H, Me), 7.79 (overlapped triplets, 2H), 8.02 (d, 1H), 8.07 (d, 1H), 8.12 (d, 1H), 8.20 (d, 1H), 8.84 (br q, NH), 9.15 (br q, NH); ^{13}C NMR (CD$_3$OD, 75.4 MHz) δ 32.44, 116.87, 125.24, 125.80, 127.24, 128.16, 128.48, 129.84, 130.65, 135.24, 135.38, 140.17, 146.15, 176.13, 183.64; ES$^+$ MS C$_{16}$H$_{14}$N$_6$S$_2$Zn (418.0) m/z 419.3 [M + H]$^+$; Anal. calcd. for C$_{16}$H$_{14}$N$_6$S$_2$Zn.H$_2$O: C 43.89, H 3.68, N 19.19; found C 44.01, H 3.88, N 19.18; IR (KBr, ν/cm^{-1}): 3435 (s broad, NH) 3347 (s broad, N–H), 2931 (w), 1569 (vs, C=N), 1384 (s, thioamide), 1064 (N–N), 774 (w, C–S). UV–Vis (DMSO) λ/nm (ε/M^{-1}cm^{-1}): 359 (4.24×10^4); 402 (1.23×10^4); 424 (1.23×10^4); 454 (1.10×10^4); 483 (1.20×10^4).

Zinc diacetyl-2-bis[4-*N*-(2´-(piperidine-1-yl)ethyl)-3-thiosemicarbazone] (ZnL^1)—yield = 74%; ^{1}H NMR (DMSO-d_6, 300 MHz) δ 1.37 (m, 4H), 1.48 (t, 8H), 2.18 (s, 6H), 2.35 (br s, 8H), 2.43 (t, 4H), 6.98 (br s, 2H, NH), 4H under residual peak of H$_2$O; ^{13}C NMR (DMSO-d_6, 75.4 MHz) δ 14.31, 23.17, 24.89, 39.02, 54.92, 58.01, 148.27, 178.77; ES$^+$ MS C$_{20}$H$_{36}$N$_8$S$_2$Zn (516.17) m/z 517.3 [M + H]$^+$; Anal. calcd. for C$_{20}$H$_{36}$N$_8$S$_2$Zn.2H$_2$O.1CH$_3$COOH: C 43.02, H 7.22, N 18.24; found C 43.20, H 6.67, N 18.34; IR (KBr, ν/cm^{-1}): 3335 (br s, N–H), 2936 (s, sharp), 1422 (vs, C=N), 1215 (s, thioamide), 1127 (N–N), 839 (w, C–S), 665 (w). UV–Vis (DMSO) λ/nm (ε/M^{-1}cm^{-1}): 263 (5.60×10^3); 314 (8.25×10^3); 438 (8.81×10^3).

Zinc diacetyl-2-bis[4-*N*-(3´-morpholinoethyl)-3-thiosemicarbazone] (ZnL^2)—yield= 76%; ^{1}H NMR (DMSO-d_6, 300 MHz) δ 2.18 (s, 6H), 2.39 (br t, 8H), 2.47 (m, 4H), 3.45 (m, 4H), 3.56 (br t, 8H), 7.01 (br s, 2H, NH); ^{13}C NMR (DMSO-d_6, 75 MHz) δ 14.02, 53.34, 57.16, 66.36, 145.30, 175.26 (gHSQC experiment revealed the presence of a signal under DMSO); ES$^+$ MS for C$_{18}$H$_{32}$N$_8$O$_2$S$_2$Zn (520.14) m/z 543.1 [M + Na]$^+$; Anal. calcd. for C$_{18}$H$_{32}$N$_8$S$_2$O$_2$Zn.4H$_2$O: C 39.24, H 6.79, N 18.86; found C 39,20, H 7.25, N 18.79; IR (KBr, ν/cm^{-1}): 3356 (vs, broad, N–H), 2936 (w), 2860 (w), 1456 (vs, C=N), 1230 (m, thioamide), 1116 (vs, N–N), 865 (w, C–S). UV–Vis (DMSO) λ/nm (ε/M^{-1}cm^{-1}): 265 (7.06×10^3); 315 (1.03×10^4); 437 (1.08×10^4).

Zinc bis[4-N-(2´-(piperidine-1-yl)ethyl)-3-thiosemicarbazone] acenaphthenequinone (ZnL^3)—yield= 70%; ^{1}H NMR (DMSO-d_6, 300 MHz) δ 1.41 (m, 4H), 1.54 (m, 8H), 2.45 (m, 8H), 2.59 (q, 4H), 3.56 (m, 4H), 7.67 (m, 2H), 7.91–7.85 (m, 2H + NH), 7.97 (d ^{3}J = 15 Hz, 1H), 8.44 (br t, 1H, NH), 8.56 (d, ^{3}J = 6 Hz, 1H); ^{13}C NMR (DMSO-d_6, 75 MHz) δ 21.34, 24.00, 25.60, 25.68, 40.96, 42.61, 54.02, 54.13, 56.72, 57.32, 116.68, 125.38, 125.50, 127.31, 128.16, 128.28, 129.89, 130.61, 135.28, 140.31, 146.25, 172.55, 175.94, 182.64. ES$^+$ MS for C$_{28}$H$_{36}$N$_8$S$_2$Zn (612.18) m/z: 613.3 [M + H]$^+$. Anal. calcd. for C$_{28}$H$_{36}$N$_8$S$_2$Zn×2CH$_3$COOH.2H$_2$O: C 49.80, H 6.28, N 14.55; found C 49.68, H 6.43, N 14.53; IR (KBr, ν/ cm^{-1}): 3277 (s broad, N–H), 2933 (w), 2860 (w), 1575 (s, C=N), 1513 (vs, C=N), 1444 (ring), 1417 (ring), 1263 (s, thioamide), 1155 (vs, N–N), 1110, 780 (w, C–S), 667. UV–Vis (DMSO) λ/nm (ε/M^{-1}cm^{-1}): 361 (2.99×10^4); 404 (9.71×10^3); 425 (9.60×10^3); 456 (9.11×10^3); 485 (9.75×10^3).

Zinc bis[4-*N*-(3´-morpholinoethyl)-3-thiosemicarbazone] acenaphthenequinone (ZnL^4)— yield= 76%; ^{1}H NMR (DMSO-d_6, 300 MHz) δ 2.46 (m, 8H), 2.61 (m, 4H), 3.63 (m, 8H), 3.72 (q, ^{3}J = 4 Hz, ^{3}J = 8 Hz, 4H), 7.68 (t, ^{3}J = 8 Hz, 2H), 7.89 (m, 2H + NH), 7.98 (d, ^{3}J = 8 Hz, 1H), 8.46 (br t, NH), 8.56 (d, ^{3}J = 8 Hz, 1H). ^{13}C NMR (DMSO-d_6, 75 MHz) δ 39.52 (signal under residual DMSO as confirmed by COSY), 42.57, 53.54, 56.62, 57.42, 66.51, 93.31, 116.97, 125.60, 127.59, 128.42, 130.05, 130.76, 135.40, 140.55, 146.33, 175.98, 182.78; ES$^+$ MS for C$_{26}$H$_{32}$N$_8$O$_2$S$_2$Zn (616.14) m/z: 617.2 [M + H]$^+$; Anal. calcd. for C$_{26}$H$_{32}$N$_8$O$_2$S$_2$Zn: C 50.52, H 5.22, N 18.13; found C 50.47, H 5.61, N 18.18; IR (KBr, ν/cm^{-1}): 3390 (s broad, N–H), 2960 (w), 2817 (w), 1575 (s, C=N), 1540 (vs, C=N), 1479 (ring), 1472 (ring), 1335 (vs, thioamide), 1119 (vs, N–N), 777 (s, C–S). UV–Vis (DMSO) λ/nm (ε/M^{-1}cm^{-1}): 361 (4.12×10^4); 403 (1.21×10^4); 424 (1.22×10^4); 453 (1.14×10^4); 486 (1.29×10^4).

Crystal structure determination

Brown crystals of **ZnL^2** and yellow–brown crystals of **ZnL^3** suitable for X-ray diffraction studies were obtained by slow diffusion of diethyl ether into concentrated methanolic or dichloromethane solutions of the complexes, respectively, after standing for several days at RT. The crystals were mounted on a loop with protective oil. X-ray data were collected at 150 K on a Bruker APEX II CCD diffractometer using graphite monochromated Mo Kα radiation (0.71073°A) and operating at 50 kV and 30 mA. The X-ray data collection was monitored by the APEX2 program. All data were corrected for Lorentzian, polarization, and absorption effects using SAINT [37] and SADAB [38] programs. Structure solution and refinement were performed using

direct methods with program SIR9 [39] and SHELXL97 [40] both included in the package of programs WINGX-Version 2014.1 [41]. A full-matrix least-squares refinement was used for the non-hydrogen atoms with anisotropic thermal parameters. All hydrogen atoms were inserted in idealized positions and allowed to refine riding in the parent atom, except the nitrogen (N3 and N6) hydrogen atoms that were finding in the electron density map and refined isotropically. Molecular graphics were prepared using Mercury [42]. CCDC—$\mathbf{ZnL^2}$-1478469 and $\mathbf{ZnL^3}$-565108—contain the supplementary crystallographic data for this paper. These data can be obtained from The Cambridge Crystallographic Data Centre via www.ccdc.cam.ac.uk/data_request/cif.

Fluorescence spectroscopy

Dimethyl sulfoxide (DMSO) was purchased from Riedel-de Haën, spectroscopy grade, and used without further purification. The complexes were dissolved in DMSO ensuring that the absorbance values remained below 0.4 at the excitation and emission wavelengths. Fluorescence measurements were carried out in 1 cm quartz cuvettes. The experiments were carried out at room temperature and using the software FluorEssence V3.

The fluorescence quantum yield of each compound was determined by the relative method, using quinine sulphate as standard [32]. To minimize instrumental errors, sample and standard solutions were prepared with very similar absorption values at the common excitation wavelength (370 nm). The fluorescence quantum yield of each complex was measured in DMSO, at room temperature. It can be calculated from Eq. 1:

$$\Phi_\mathrm{f}^i = \frac{F^i f_\mathrm{S} \eta_i^2}{F^S f_i \eta_\mathrm{S}^2} \Phi_\mathrm{f}^S, \tag{1}$$

where Φ_f^i and Φ_f^s are the fluorescence quanta yield of the sample and standard, respectively. F^i and F^s are the integrated intensities (areas) of sample and standard spectra, respectively (in units of photons); f_x is the absorption factor, or the fraction of the light reaching the sample that is absorbed ($f_x = 1-10^{-Ax}$, where $A =$ absorbance); η_i and η_s are the refractive indices of the sample and reference solution, respectively [32].

Fluorescence average lifetimes were determined by single-photon counting technique. Good to fit values (χ^2) were found between 0.79 and 0.99.

Cell culture

Human ovarian epithelial cancer A2780 (cisplatin sensitive) and A2780R (acquired cisplatin resistance) as well as prostate carcinoma PC3 and LNCap cell lines were maintained in RPMI 1640 Medium. Human breast carcinoma MCF7, cervical carcinoma HeLa cells and the non-tumoral HEK 293 (human embryonic kidney) cells were grown in DMEM. Both culture media were supplemented with 10% heat-inactivated fetal bovine serum (FBS). All culture media and supplements were from Gibco, Invitrogen, UK. Cells were cultured in a humidified atmosphere of 95% air and 5% CO_2 at 37 °C (Heraeus, Germany).

Cytotoxicity assay

The cytotoxicity of the BTSC chelators and corresponding Zn(II) complexes was assessed by evaluating their effects on cellular proliferation using the [1-(4,5-dimethylthiazol-2-yl)-2,5-diphenyl tetrazolium] (MTT) assay. Cells were seeded in 96-well culture plates at a density of 1.5×10^4 to 2.5×10^4 cells/well (depending of the cell line) and left to adhere overnight at 37°C. Cells were then incubated with the Zn complexes and respective ligands at different concentrations (0–50 μM) during 48 h at 37°C. All tested compounds were first solubilized in DMSO (20 mM stock solution) and then diluted in culture medium for the assay, with the percentage of organic solvent in the final solution never exceeding 0.1%. After incubation, the medium was removed, cells washed with PBS and then incubated with MTT (200 μL of 0.5 mg/mL solution in Modified Eagle's Medium without phenol red) for 3 h at 37°C. The MTT solution was then removed and the insoluble blue formazan crystals formed were dissolved in DMSO. The absorbance of this colored (purple) solution was measured at 570 nm, using a plate spectrophotometer (Power Wave Xs; Bio-Tek). Each test was performed with at least six replicates. The results were expressed as percentage of the surviving cells in relation with the control, which was incubated without any compound. IC_{50} values were determined using Graph Pad Prism.

Zn determination by ICP-MS

Cellular uptake of the zinc complexes was assessed by ICP-MS quantification of total zinc. Adherent and confluent MCF7 cells (T25 culture flask) were incubated with the tested compounds (10 μM) or with DMSO as control in culture medium for 30 min and 2 h at 37 °C and 5% CO_2. The harvested cell suspension was centrifuged at 200 g for 3 min at 4º C (Centrifuge 5804R, Eppendorf) and cells washed twice with cold PBS to remove the unbound complex. An aliquot of 10 mL of cells suspension was separated for counting the number of cells with trypan blue. Cell pellets were resuspended in 100 μL of concentrated nitric acid (65% HNO_3, Merck) purified by sub-boiling distillation (bi-distilled) and left to digest overnight. Samples were then heated for 20 min at 90 °C (in a sand bath) to complete

the digestion. To each sample was added 1.5 mL of 1% (v/v) nitric acid diluted with water ultra-pure (18.2 MΩcm) obtained with a MilliQ water purification system (Millipore). All samples were filtered with a 0.45 µm PVDF membrane syringe filter. Samples were 4 times diluted with H_2O ultra-pure before their Zn content was determined by ICP-MS. SmartTune Solution-Std Elan & DRC-e and ELAN 100 Set up/Stab/MassCal standards solutions by Perkin Elmer Pure Atomic Spectroscopy Standard were used for daily and monthly optimization and tuning. Measurement sequences began with blank and standard solutions.

The instrument was calibrated using 0, 5, 10, 50, 100 and 500 parts per billion (ppb) of certified Calibration Standard 3 solution (Perkin Elmer) prepared in 1% (v/v) nitric acid. To minimize drift effects, instruments instability and matrix effects, a certified internal standard solution containing 200 ppb of rhodium (Rh) was added to each sample and standard solution. Detection limit (0.22 ppb) was determined based on the low range concentrations of the standards used. The concentration of Zn was calculated as ng of metal per million of cells.

Live-cell fluorescence microscopy—cellular uptake studies

Cellular uptake of the zinc complexes was measured by fluorescence microscopy using the compounds' intrinsic fluorescence. MCF7 cells were plated in 8-well chambered slides (Millicell EZ slide, Millipore) (20000 cells/well) in DMEM Fluorobrite supplemented with 10% FBS (Gibco) and allowed to attach overnight. The following day cell nuclei were stained by incubating the vital dye Hoechst 33342 (0.2 µg/ml) in the culture media for 30 min. After that period, the culture medium was replaced by fresh medium containing the compounds (10 or 20 µM) or an identical amount of DMSO (0.1%) as control. Then, cells were immediately placed in an automated Leica DMI 6000B widefield fluorescence microscope for live-cell imaging. Cells were imaged every 5 min during approximately 60 min using a $10 \times$ objective with numerical aperture 0.4. Three image channels were acquired: Bright field (transmission), Hoechst fluorescence (excitation band: 340–380 nm; emission band: 450–490 nm) and compound fluorescence (excitation band: 490–510 nm; emission band: 520–550 nm). Cells were kept at 37 °C and 5% CO_2 throughout all steps of the protocol, except when adding compounds or the nuclear dye.

Accumulation of the compounds by individual cells was measured with an automatic image analysis algorithm implemented in CellProfiler [43]. Briefly, the Hoechst staining was used to segment individual nuclei. Then, the nuclear shape was dilated by 7.8 µm to estimate the location of the whole cell. Finally, the mean compound fluorescence in the cell objects was measured, after adequate background subtraction. Each condition was imaged in duplicate, with ~ 60–80 cells being analyzed for each condition (minimum of 40 cells per condition). Values were reported as the average compound fluorescence $\pm$ standard deviation across the 2 time lapses at each timepoint.

Live-cell fluorescence microscopy—co-localization studies

For the co-localization studies, cells were plated as mentioned above. The day of the assay, cells were loaded with the vital dye Hoechst 33342 (0.2 µg/ml) to stain the nuclei and Lysotracker Red DND-99 (50 nM) to stain the lysosomes in DMEM Fluorobrite for 30 min. After that period, the culture medium was replaced by fresh medium containing **ZnL³** or **ZnNqTSM^asym** (20 µM) or an identical amount of DMSO (0.1%) as control. Then, cells were immediately placed in an automated Leica DMI 6000B widefield fluorescence microscope for live-cell imaging. Cells were imaged at 0, 15, and 30 min using a 10x objective with numerical aperture 0.4. Three image channels were acquired: Bright field (transmission), Hoechst fluorescence (excitation band: 340–380 nm; emission band: 450–490 nm), **ZnL³**, or **ZnNqTSM^asym** fluorescence (excitation band: 490–510 nm; emission band: 520–550 nm) and Lysotracker fluorescence (excitation band: 515–560 nm; emission band: > 590 nm). Cells were kept at 37 °C and 5% CO_2 throughout all steps of the protocol, except when adding compounds or the nuclear dye.

Lysosomal membrane permeabilization assay

The ability of the selected compounds to induce LMP was assessed according to Acridine Orange (AO; Sigma-Aldrich) distribution. MCF7 cells were seeded on sterile coverslips to give 50% confluency and left to adhere overnight. Cells were then incubated with AO (5 µg/mL) for 15 min at 37 °C, washed 3 times with PBS, and then incubated for 1 h at 37 °C with **H₂L³** or **ZnL³** (10 µM). The cells were then washed 3 times with PBS, fixed with 4% formaldehyde in PBS for 20 min at room temperature and coverslips mounted in mounting media (Fluoroshield with DAPI, Sigma). Images were captured using a Zeiss Axioplan2 microscope equipped with FITC and Texas Red filters. Several images were randomly collected in each slide. The red and green fluorescence intensities were quantified with image processing and analysis software (ImageJ v1.51 k), and presented as red/green ratio normalized to the control.

Intracellular ROS production assay

Intracellular ROS generation was measured using 2′,7′-dichlorodihydrofluorescein diacetate (H₂DCF-DA,

ThermoFisher Scientific). H$_2$DCF-DA is hydrolyzed by intracellular esterases to the membrane impermeable analog, 2′,7′-dichlorodihydrofluorescein (H$_2$DCF), which leads to its accumulation within the cytosol. Cellular oxidants localized in the cytosol, such as H$_2$O$_2$, HO·, ROO·, or ONOO$^-$, oxidize non-fluorescent H$_2$DCF to the fluorescent product, dichlorofluorescin (DCF).

H$_2$DCF-DA stock solution (10 mM) in DMSO was stored at −20 °C. MCF7 cells were seeded on sterile coverslips to give 50% confluency and left to adhere overnight. Cells were incubated with **H$_2$L^3** and **ZnL^3** (2, 10, and 20 µM) in MEM (without phenol red, Gibco) supplemented with 10% FBS (assay medium) for 30 min at 37 °C, in the dark, and then washed once with assay medium. Subsequently, H$_2$DCF-DA (1 µM) in assay medium was added for further 30 min. Hydrogen peroxide (H$_2$O$_2$, 3% (10 vol)), 5 times diluted in assay medium, was used as a positive control. After incubation, cells were washed with MEM, and fixed with 4% formaldehyde in PBS, for 20 min at room temperature. Cells were finally mounted in mounting media (Fluoroshield with DAPI, Sigma). Images were captured using a Zeiss Axioplan2 microscope equipped with FITC filter. Several images were randomly collected in each slide. Green cytosolic DCF fluorescence intensity is directly proportional to intracellular ROS generated and was quantified with ImageJ v1.51 k. Fluorescence intensity data were normalized to the control (H$_2$DCF-DA only).

References

1. Santini C, Pellei M, Gandin V, Porchia M, Tisato F, Marzano C (2014) Advances in copper complexes as anticancer agents. Chem Rev 114(1):815–862

2. Shuhong C, Xiahui C, Ligen C, Jingwen C (2016) α(N)-Heterocyclic thiosemicarbazones: iron chelators that are promising for revival of gallium in cancer chemotherapy. Anti-Cancer Agents Med Chem 16(8):973–991

3. Stacy AE, Palanimuthu D, Bernhardt PV, Kalinowski DS, Jansson PJ, Richardson DR (2016) Zinc(II)–thiosemicarbazone complexes are localized to the lysosomal compartment where they trans-metallate with copper ions to induce cytotoxicity. J Med Chem 59(10):4965–4984

4. Park KC, Fouani L, Jansson PJ, Wooi D, Sahni S, Lane DJR, Palanimuthu D, Lok HC, Kovacevic Z, Huang MLH, Kalinowski DS, Richardson DR (2016) Copper and conquer: copper complexes of di-2-pyridylketone thiosemicarbazones as novel anti-cancer therapeutics. Metallomics 8(9):874–886

5. Cortezon-Tamarit F, Sarpaki S, Calatayud DG, Mirabello V, Pascu SI (2016) Applications of "hot" and "cold" bis(thiosemicarbazonato) metal complexes in multimodal imaging. Chem Rec 16(3):1380–1397

6. Dehdashti F, Mintun MA, Lewis JS, Bradley J, Govindan R, Laforest R, Welch MJ, Siegel BA (2003) In vivo assessment of tumor hypoxia in lung cancer with 60Cu-ATSM. Eur J Nucl Med Mol Imaging 30(6):844–850

7. Holland JP, Lewis JS, Dehdashti F (2009) Assessing tumor hypoxia by positron emission tomography with Cu-ATSM. Q J Nucl Med Mol Imaging 53(2):193–200

8. Carlin S, Humm JL (2012) PET of hypoxia: current and future perspectives. J Nucl Med 53(8):1171–1174

9. Jansson PJ, Kalinowski DS, Lane DJR, Kovacevic Z, Seebacher NA, Fouani L, Sahni S, Merlot AM, Richardson DR (2015) The renaissance of polypharmacology in the development of anti-cancer therapeutics: inhibition of the "triad of death" in cancer by Di-2-pyridylketone thiosemicarbazones. Pharmacol Res 100 (Supplement:C):255–260

10. Guo Z-L, Richardson DR, Kalinowski DS, Kovacevic Z, Tan-Un KC, Chan GC-F (2016) The novel thiosemicarbazone, di-2-pyridylketone 4-cyclohexyl-4-methyl-3-thiosemicarbazone (DpC), inhibits neuroblastoma growth in vitro and in vivo via multiple mechanisms. J Hematol Oncol 9(1):98

11. Stacy AE, Palanimuthu D, Bernhardt PV, Kalinowski DS, Jansson PJ, Richardson DR (2016) Structure-activity relationships of Di-2-pyridylketone, 2-Benzoylpyridine, and 2-Acetylpyridine thiosemicarbazones for overcoming Pgp-mediated drug resistance. J Med Chem 59(18):8601–8620

12. Gutierrez EM, Seebacher NA, Arzuman L, Kovacevic Z, Lane DJ, Richardson V (2016) Lysosomal membrane stability plays a major role in the cytotoxic activity of the anti-proliferative agent, Di-2-pyridylketone 4,4-dimethyl-3-thiosemicarbazone (Dp44mT). Biochim Biophys Acta 1863:1665–1681

13. Stefani C, Al-Eisawi Z, Jansson PJ, Kalinowski DS, Richardson DR (2015) Identification of differential anti-neoplastic activity of copper bis(thiosemicarbazones) that is mediated by intracellular reactive oxygen species generation and lysosomal membrane permeabilization. J Inorg Biochem 152:20–37

14. Palma E, Mendes F, Morais GR, Rodrigues I, Santos IC, Campello MP, Raposinho P, Correia I, Gama S, Belo D, Alves V, Abrunhosa AJ, Santos I, Paulo A (2017) Biophysical characterization and antineoplastic activity of new bis(thiosemicarbazonato) Cu(II) complexes. J Inorg Biochem 167:68–79

15. Fan J, Han Z, Kang Y, Peng X (2016) A two-photon fluorescent probe for lysosomal thiols in live cells and tissues. Sci Rep 6:19562

16. Daum S, Reshetnikov MSV, Sisa M, Dumych T, Lootsik MD, Bilyy R, Bila E, Janko C, Alexiou C, Herrmann M, Sellner L, Mokhir A (2017) Lysosome-targeting amplifiers of reactive oxygen species as anticancer prodrugs. Angew Chem Int Ed Engl 56(49):15545–15549

17. Pascu SI, Waghorn PA, Conry TD, Betts HM, Dilworth JR, Churchill GC, Pokrovska T, Christlieb M, Aigbirhio FI, Warren JE (2007) Designing Zn(ii) and Cu(ii) derivatives as probes for in vitro fluorescence imaging. Dalton Trans 43:4988–4997

18. Pascu SI, Waghorn PA, Conry TD, Lin B, Betts HM, Dilworth JR, Sim RB, Churchill GC, Aigbirhio FI, Warren JE (2008) Cellular confocal fluorescence studies and cytotoxic activity of new Zn(II) bis(thiosemicarbazonato) complexes. Dalton Trans 16:2107–2110

19. Alam IS, Arrowsmith RL, Cortezon-Tamarit F, Twyman F, Kociok-Kohn G, Botchway SW, Dilworth JR, Carroll L, Aboagye EO, Pascu SI (2016) Microwave gallium-68 radiochemistry for kinetically stable bis(thiosemicarbazone) complexes: structural investigations and cellular uptake under hypoxia. Dalton Trans 45(1):144–155

20. Addison AW, Rao TN, Reedijk J, van Rijn J, Verschoor GC (1984) Synthesis, structure, and spectroscopic properties of copper(II) compounds containing nitrogen-sulphur donor ligands; the crystal and molecular structure of aqua[1,7-bis(N-methylbenzimidazol-2[prime or minute]-yl)-2,6-dithiaheptane]copper(II) perchlorate. J Chem Soc, Dalton Trans 7:1349–1356

21. Yang W, Ma Z, Yi J, Sun W-H (2017) Quantitative structure-thermostability relationship of late transition metal catalysts in ethylene oligo/polymerization. Catalysts 7(4):120

22. López-Torres E, Mendiola MA, Rodríguez-Procopio J, Sevilla MT, Colacio E, Ma Moreno J, Sobrados I (2001) Synthesis and characterisation of zinc, cadmium and mercury complexes of benzilbisthiosemicarbazone. Structure of cadmium derivative. Inorg Chim Acta 323(1):130–138

23. Christlieb M, Holland JP, Dilworth JR (2010) Investigation of the UV–Vis absorption of bis(N-methylthiosemicarbazonato) zinc Zn[ATSM]. Inorg Chim Acta 363(6):1133–1139

24. Cowley AR, Davis J, Dilworth JR, Donnelly PS, Dobson R, Nightingale A, Peach JM, Shore B, Kerr D, Seymour L (2005) Fluorescence studies of the intra-cellular distribution of zinc bis(thiosemicarbazone) complexes in human cancer cells. Chem Commun 7:845–847

25. Holland JP, Aigbirhio FI, Betts HM, Bonnitcha PD, Burke P, Christlieb M, Churchill GC, Cowley AR, Dilworth JR, Donnelly PS, Green JC, Peach JM, Vasudevan SR, Warren JE (2007) Functionalized Bis(thiosemicarbazonato) complexes of zinc and copper: synthetic platforms toward site-specific radiopharmaceuticals. Inorg Chem 46(2):465–485

26. Brown OC, Tocher DA, Blower PJ, Went MJ (2015) Crystal structure of [butane-2,3-dione bis-(4-methyl-thio-semicarbazonato)-kappa(4) S, N (1), N (1′), S'](pyridine-kappaN)zinc(II). Acta Crystallogr, Sect E: Crystallogr Commun 71(Pt 11):1349–1351

27. Blower PJ, Castle TC, Cowley AR, Dilworth JR, Donnelly PS, Labisbal E, Sowrey FE, Teat SJ, Went MJ (2003) Structural trends in copper(II) bis(thiosemicarbazone) radiopharmaceuticals. Dalton Trans 23:4416–4425

28. West DX, Ives JS, Bain GA, Liberta AE, ValdesMartinez J, Ebert KH, HernandezOrtega S (1997) Copper(II) and nickel(II) complexes of 2,3-butanedione bis(N(3)-substituted thiosemicarbazones). Polyhedron 16(11):1895–1905

29. West DX, Liberta AE, Padhye SB, Chikate RC, Sonawane PB, Kumbhar AS, Yerande RG (1993) Thiosemicarbazone complexes of copper(II)—structural and biological studies. Coordin Chem Rev 123(1–2):49–71

30. Gonzalez-Garcia C, Mendiola MA, Perles J, Lopez-Torres E (2017) Structural diversity and supramolecular architectures of Zn(II), Cu(II) and Ni(II) complexes by selective control of the degree of deprotonation of diacetyl bis(4-isopropyl-3-thiosemicarbazone). CrystEngComm 19(7):1035–1044

31. Shao J, Ma ZY, Li A, Liu YH, Xie CZ, Qiang ZY, Xu JY (2014) Thiosemicarbazone Cu(II) and Zn(II) complexes as potential anticancer agents: syntheses, crystal structure, DNA cleavage, cytotoxicity and apoptosis induction activity. J Inorg Biochem 136:13–23

32. Brouwer Albert M (2011) Standards for photoluminescence quantum yield measurements in solution (IUPAC Technical Report). Pure Appl Chem 83(12):2213

33. Eaton DF (1988) Reference materials for fluorescence measurement. Pure Appl Chem 60(7):1107

34. Hashemi M, Ghavami S, Eshraghi M, Booy EP, Los MJ (2007) Cytotoxic effects of intra and extracellular zinc chelation on human breast cancer cells. Eur J Pharmacol 557(1):9–19

35. Gomes A, Fernandes E, Lima JL (2005) Fluorescence probes used for detection of reactive oxygen species. J Biochem Biophys Methods 65(2–3):45–80

36. Cesen MH, Pegan K, Spes A, Turk B (2012) Lysosomal pathways to cell death and their therapeutic applications. Exp Cell Res 318(11):1245–1251

37. SMART, SAINT and SADABS (2005) Bruker AXS Inc., Madison, Wisconsin, USA. SMART, SAINT and SADABS

38. Sheldrick SGM (2004) Bruker AXS Inc. Madison, Wisconsin, USA

39. Altomare A, Burla MC, Camalli M, Cascarano GL, Giacovazzo C, Guagliardi A, Moliterni AGG, Polidori G, Spagna R (1999) SIR97: a new tool for crystal structure determination and refinement. J Appl Crystallogr 32(1):115–119

40. Sheldrick GM (2008) A short history of SHELX. Acta Crystallogr Sect A: Found Crystallogr 64(Pt 1):112–122

41. Farrugia L (2012) WinGX and ORTEP for Windows: an update. J Appl Crystallogr 45(4):849–854

42. Macrae CF, Bruno IJ, Chisholm JA, Edgington PR, McCabe P, Pidcock E, Rodriguez-Monge L, Taylor R, van de Streek J, Wood PA (2008) Mercury CSD 2.0—new features for the visualization and investigation of crystal structures. J Appl Crystallogr 41(2):466–470

43. Carpenter AE, Jones TR, Lamprecht MR, Clarke C, Kang IH, Friman O, Guertin DA, Chang JH, Lindquist RA, Moffat J, Golland P, Sabatini DM (2006) Cell profiler: image analysis software for identifying and quantifying cell phenotypes. Genome Biol 7(10):R100